

# X-Splat: Gaussian Splatting for 3D CBCT Generation from Single Panoramic Radiograph

Tomasz Szczepański<sup>1,\*</sup> Szymon Płotka<sup>2</sup> Michał K. Grzeszczyk<sup>1</sup>  
Tomasz Trzeciński<sup>3,4</sup> Arkadiusz Sitek<sup>5</sup>

<sup>1</sup>Sano Centre for Computational Medicine, Poland <sup>2</sup>Jagiellonian University, Poland

<sup>3</sup>Warsaw University of Technology, Poland <sup>4</sup>Research Institute IDEAS, Poland

<sup>5</sup>Harvard Medical School, USA

Generating a 3D dental volume from a single panoramic radiograph (PXR) could provide a low-radiation alternative to Cone-Beam Computed Tomography (CBCT), but the problem is highly underdetermined: panoramic acquisition integrates 3D attenuation along curved X-ray paths into a 2D image, leaving depth-resolved anatomy unobserved. Existing implicit and generative approaches often produce oversmoothed geometry or anatomically inconsistent hallucinations, lacking geometry-driven supervision and relying on smooth representations unable to precisely localize sharp anatomical boundaries. We propose X-Splat, the first Gaussian Splatting framework for generating CBCT-like 3D dental volumes from a single PXR. X-Splat uses the known panoramic acquisition geometry as a generation scaffold: learnable anisotropic Gaussian primitives are initialized along the X-ray paths that formed the input image and adjusted in a single feed-forward pass, constrained by Beer–Lambert reprojection and multi-view radiographic training supervision. A lightweight residual refiner adds dataset-level anatomical priors without overriding the geometry already resolved by the Gaussians. We train on synthetic PXR–CBCT pairs, enabling direct volumetric supervision without paired real scans. We further introduce segmentation-based geometry-aware metrics, providing the first evaluation of PXR-based generation over maxillofacial anatomy. X-Splat outperforms NeRF- and GAN-based baselines, recovering individual teeth, cortical boundaries, and alveolar structure, including the mandibular canal which prior methods fail to reconstruct. Code will be available at [github.com/X-Splat](https://github.com/X-Splat).

## 1. Introduction

Inferring 3D anatomy from 2D projections is a fundamental problem across imaging science, physics, and computer vision, with particular clinical importance in dentistry, where

Cone-Beam Computed Tomography (CBCT) remains the standard for 3D maxillofacial imaging by acquiring hundreds of 2D projections over a full arc to reconstruct a sub-millimetre attenuation volume [37]. Its diagnostic superiority over 2D imaging is well established, from detecting cortical destruction and root resorption to depicting the relationship between molar roots and the mandibular canal [44]. Yet CBCT is acquired only when clinically indicated, whereas panoramic radiography (PXR) is widely available, low-cost, and substantially lower in radiation dose [32, 34]. Consequently, routine dental care often produces longitudinal archives of panoramic images, while CBCT data remain comparatively sparse. Inferring a CBCT-like volume from a single PXR would extend 3D dental analysis to large retrospective panoramic-image archives and to settings where CBCT is unavailable [25, 28]. However, the problem is a highly underdetermined inverse problem: a panoramic projection integrates 3D attenuation along rays into a single 2D image, leaving depth-resolved anatomy unobserved (Fig.1). Unlike sparse-view CT, where multiple projections constrain depth [19, 46, 47], generating a 3D volume from a single-view requires strong anatomical and geometric priors as necessary constraints.

Existing PXR-to-3D methods [15, 17, 24, 30, 31, 38] leave three gaps that motivate our work. First, they rely on convolutional encoder-decoders or implicit neural fields that represent the volume as a dense grid or continuous scalar field; such representations are smooth by construction and systematically under-resolve the sharp interfaces, such as root boundaries, cortical bone surfaces, and the mandibular canal cortex, that carry the most diagnostic value. Implicit paradigms like NeRF [27] sample at fixed intervals along each ray and cannot adapt to anatomical structure, while GAN-[10, 45] and diffusion-based [12, 42] generators risk anatomically inconsistent hallucinations and often remain computationally prohibitive at CBCT resolu-

\*t.szczepanski@sanoscience.org

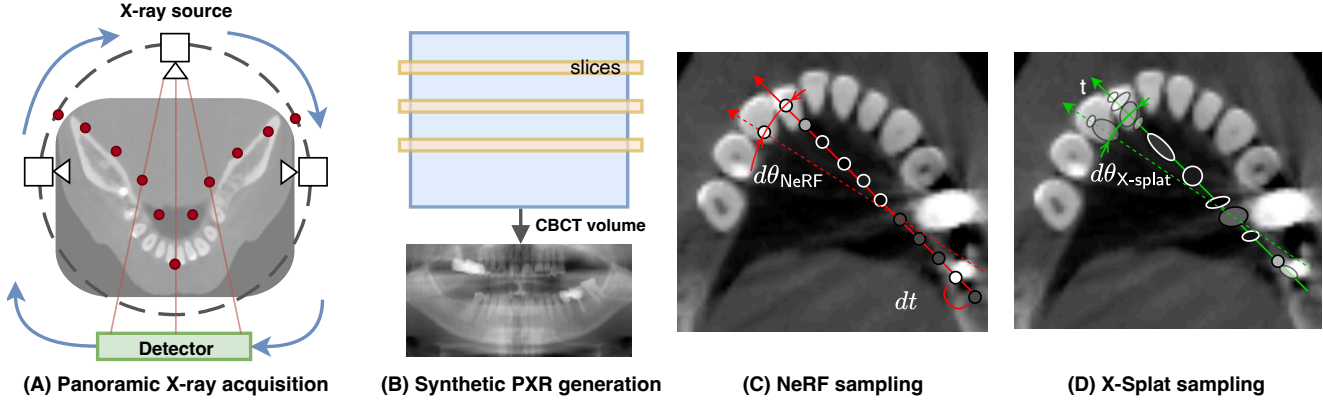


Figure 1. (A) A panoramic X-ray (PXR) is acquired by rotating an X-ray source and detector around the patient’s head, producing a single 2D projection encoding the full dental anatomy. (B) Synthetic PXRs are generated from a CBCT volume by casting rays through axial slices and accumulating attenuation according to Beer-Lambert law. (C) NeRF-based generation samples points at fixed intervals along each ray  $dt$ , unable to adapt to anatomical structure and leaving gaps between sparse rays unresolved. (D) **X-Splat** 3D Gaussians are anisotropic, learnable and parameterized along each ray  $t$ . They dynamically travel from their anchors, rotate and elongate to align with anatomical structures, efficiently filling inter-ray space.

tion. Second, prior methods either require additional input beyond the PXR, such as dental arch curves [38], or produce volumes from a single image that are locally plausible but globally inconsistent with real dental topology. Third, evaluation remains dominated by intensity-based metrics such as SSIM and PSNR, sometimes with coarse global Dice Score [31]; recent sparse-view studies show these aggregate voxel errors without reflecting whether clinically relevant structures are correctly recovered, so substantial structural inaccuracy can pass unnoticed [18]. A detailed review of related work is provided in Appendix A.

To address these limitations, we propose **X-Splat**, a Gaussian Splatting framework for single-view 3D CBCT-like volumes from a panoramic radiograph. We formulate single-PXR 3D dental volume estimation as *geometry-constrained generation*: unlike tomographic reconstruction, which resolves depth from multiple projections, a single PXR leaves the volume underdetermined, requiring conditional generation under strong geometric priors. Rather than a smooth implicit field, we represent the volume with localized anisotropic 3D Gaussian primitives [14] whose explicit geometry naturally encodes sharp boundaries and can be optimized via physics-consistent radiative rendering aligned with the Beer-Lambert attenuation model [6, 48]. Gaussians are initialized along panoramic acquisition rays and predicted in a feed-forward pass, then displaced, rotated, and anisotropically scaled to follow anatomical boundaries and fill the space between sparsely separated rays (Fig. 1D). Finally, we evaluate generated volumes’ quality using a ToothFairy3-trained segmentation network [2, 4, 5, 40, 41] to derive geometry-aware metrics over individual teeth, the mandibular canal (MC), and the

five major maxillofacial structures, providing a more faithful assessment of structural fidelity than intensity measures alone. Our main contributions are as follows:

1. We propose **X-Splat**, the first Gaussian Splatting framework for generating CBCT-like 3D dental volumes from a single panoramic radiograph. Explicit anisotropic Gaussian primitives, constrained by Beer-Lambert re-projection and multi-view radiographic supervision, provide a geometry-grounded alternative to the smooth implicit fields and dense voxel decoders of prior PXR-to-3D methods.
2. From a single PXR alone, X-Splat recovers fine dental and maxillofacial structures that existing methods systematically miss, including individual tooth roots, cortical boundaries, and the mandibular canal. This is enabled by a ray-anchored Gaussian representation in which a shared feed-forward network predicts each primitive’s displacement, orientation, scale, and density using the known panoramic acquisition geometry as an acquisition scaffold.
3. We combine geometry-driven Gaussian generation with a lightweight residual refiner constrained by multi-view DRR supervision, adding dataset-level anatomical detail while keeping the generated volume tied to the input projection. We further introduce geometry-aware structural metrics beyond conventional image-quality measures, evaluating recovery of individual teeth, cortical boundaries, alveolar structure, and the mandibular canal.

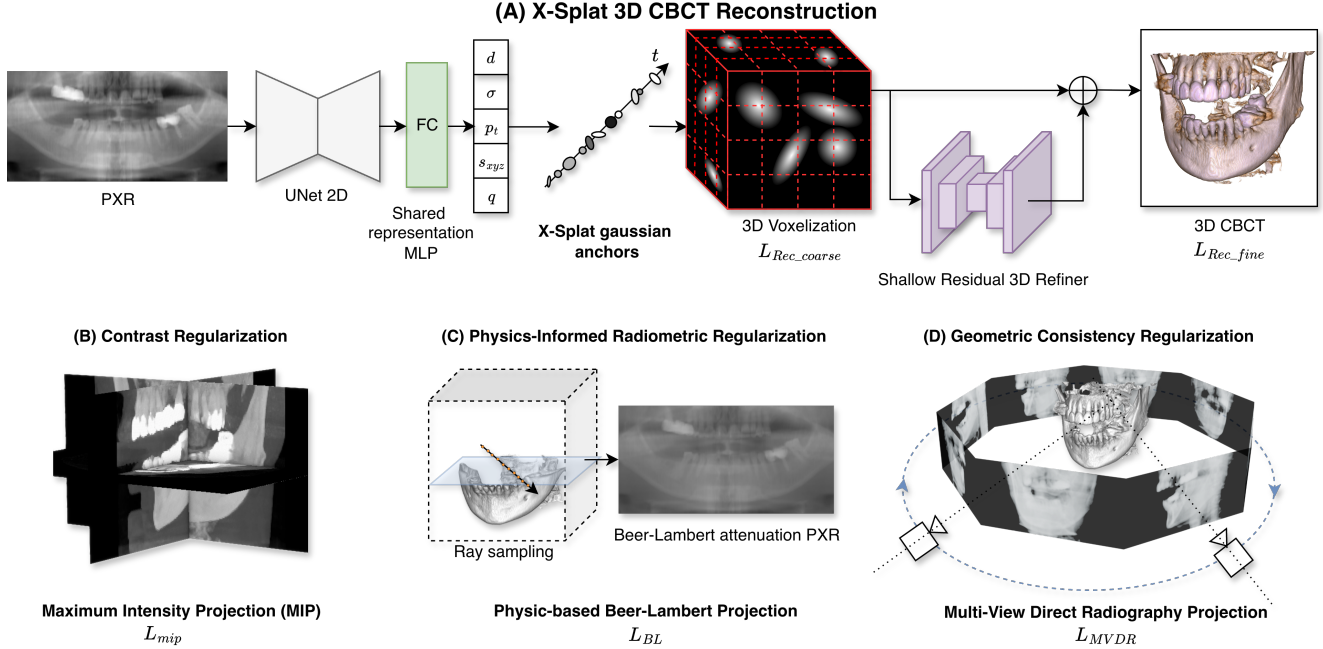


Figure 2. **Method overview and regularization scheme.** (A) A single panoramic X-ray (PXR) is processed by a 2D U-Net encoder and shared MLP to predict a set of 3D Gaussians, which are voxelized into a coarse CBCT volume. A residual 3D U-Net refiner then produces the final volume. Both the coarse and refined volumes are supervised with three regularizations: (B) Contrast Regularization (MIP-based), (C) Radiometric Regularization (Beer-Lambert law), and (D) Geometric Regularization (multi-view ray consistency). The refined volume is additionally supervised via perceptual loss on its 2D projections.

## 2. Methods

We design X-Splat using three complementary choices. **(i) Geometry-anchored initialization:** we exploit the known panoramic acquisition geometry, anchoring 3D Gaussian primitives along the predefined ray trajectories that map 2D pixels to 3D space, concentrating capacity where the input is informative without per-scene optimization. **(ii) Feed-forward prediction and refinement:** a 2D U-Net encoder and a single MLP, shared across all Gaussian attributes and anchors, predict all Gaussian parameters from the input and each anchor’s positional encoding; the Gaussians are rasterized into a coarse volume, which a lightweight 3D residual U-Net refines, adding population-level anatomical priors as a small correction that keeps the output tethered to the input. **(iii) Multi-view consistency:** during training, additional azimuthal projections supervise the volume, contracting the feasible set toward anatomically consistent solutions. Figure 2 illustrates the pipeline; the following subsections detail each component.

### 2.1. Problem Formulation

Let  $\mathbf{I} \in \mathbb{R}^{H_p \times W_p}$  denote a simulated panoramic X-ray (SimPX) rendered from a ground-truth CBCT volume  $V^* \in \mathbb{R}^{H \times W \times D}$  using the panoramic ray geometry and effective Beer-Lambert rendering convention of NeBLa [31].

This provides a calibrated computational forward model of panoramic image formation in which scanner-dependent spectral and intensity effects are absorbed into effective attenuation and rendering parameters. For a ray  $\mathbf{r}(t)$ , the projected intensity is:

$$\mathcal{F}(V, \theta)(h, w) = \frac{1 - I_0 \exp\left(-\beta \sum_k \mu_k \Delta s\right)}{p_{\max}}, \quad (1)$$

where  $\mu_k$  denotes the effective attenuation at sample  $k$  along the ray,  $\Delta s$  is the voxel step size, and  $I_0$ ,  $\beta$ , and  $p_{\max}$  are calibrated rendering constants. The inverse problem is to recover  $\hat{V}$  from a single observation  $\mathbf{I} = \mathcal{F}(V^*, \theta_0)$ .

### 2.2. SimPX Ray Geometry

We adopt the SimPX synthesis pipeline and focal-trough ray geometry from NeBLa [31]. The panoramic focal trough is modelled by a quadratic curve  $f(x) = 0.01(x \pm 100)^2$ , where  $x$  denotes horizontal coordinate in the axial CBCT slice, that defines 21 rotation centers: (see Fig.1 (A))  $\mathbf{c}_i$ ,  $i = 0, \dots, 20$ , placed on the axial plane of a  $256 \times 256$  CBCT slice. At each centre  $\mathbf{c}_i$ , rays are rotated by an angle  $\theta_i$  that varies with the dental region (denser near the molars) to simulate the variable angular sweep of a real panoramic scanner. Along each ray,  $K = 200$  points are uniformly

sampled within the volume boundary and rendered to a single pixel via Eq. (1). The resulting SimPX has  $H_p$  rows (one per CBCT slice in  $Z$ ) and  $W_p$  columns equal to the total number of rays, producing a 2D image whose pixels map to known 3D ray trajectories. This explicit ray-pixel correspondence is the geometric prior that X-Splat exploits for anchor placement, as described next.

### 2.3. Gaussian Anchor Initialization

The ray geometry provides a uniquely informative spatial prior. Every pixel  $(h, w)$  of the SimPX corresponds to a known 3D ray  $\mathbf{r}_{h,w}(t)$ , and the pixel intensity encodes the integrated attenuation along that ray. Rather than learning anchor positions from scratch through adaptive densification, we exploit this prior directly: we place one Gaussian anchor per ray sample, yielding  $N_g \approx 6\text{M}$  anchors  $\{\mathbf{p}_j\}_{j=1}^{N_g}$  that densely cover the dental arch and jaw region from the outset. This concentrates representational capacity where the input is informative, avoiding the costly exploration phase that unconstrained Gaussian methods require.

### 2.4. 3D Gaussian Splatting

**Shared MLP.** A single MLP  $f_\phi$ , shared across all  $N_g$  anchors, predicts each Gaussian’s displacement, scale, rotation, and density in one forward pass. We extend the MLP conditioning scheme of NeBLa [31], combining global image features with per-point positional encoding, to the Gaussian Splatting domain. Per-scene optimization methods solve these jointly through iteration with adaptive densification and non-uniform learning rates per attribute [14, 48]; our feed-forward setting must resolve all parameters simultaneously and uniformly from the input image alone. Sharing weights across anchors is key: rather than predicting each attribute through separate heads, the network builds joint inductive biases over the full anatomy, since tissue of a given density at a given location implies a characteristic scale and orientation, which would be underexploited with a multi-head design. The MLP predicts:

$$(\hat{\delta}t_j, \mathbf{s}_j, \mathbf{q}_j, \alpha_j) = f_\phi(\mathbf{F}(\mathbf{p}_j) + \text{PE}(\mathbf{p}_j)), \quad (2)$$

where  $\mathbf{F}(\mathbf{p}_j)$  are UNet features read directly at the pixel location on ray corresponding to anchor  $\mathbf{p}_j$  in the SimPX,  $\text{PE}(\mathbf{p}_j)$  is the positional encoding,  $\hat{\delta}t_j$  is a raw scalar displacement,  $\mathbf{s}_j \in \mathbb{R}^3$  the log-scale,  $\mathbf{q}_j \in \mathbb{R}^4$  a unit quaternion, and  $\alpha_j$  the density.

**Constrained axial-plane movement.** Each Gaussian is permitted to move only along its anchor ray within the axial (XY) plane. This constraint is motivated by the structure of the SimPX: because rays run perpendicular to the dental arch and the CBCT is sampled slice-by-slice along  $Z$ , allowing inter-slice ( $Z$ -axis) Gaussian migration would

corrupt the dense axial coverage. The scalar displacement is bounded by  $\delta t_j = \tanh(\hat{\delta}t_j) \cdot \delta t_{\max}$ , where  $\delta t_{\max} = 32$  vox, and projected onto a 3D offset via the ray’s axial unit direction  $\hat{\mathbf{d}}_{w_j} \in \mathbb{R}^2$ :

$$\Delta \mathbf{p}_j = \left[ \delta t_j \cdot \frac{\hat{\mathbf{d}}_{w_j}}{\mathbf{h}_{XY}}, 0 \right], \quad (3)$$

where  $\mathbf{h}_{XY} = [H/2, W/2]$  maps voxel displacement to the  $[-1, 1]^3$  coordinate system and the zero  $Z$ -component enforces the no-inter-slice constraint. The final Gaussian centre is  $\tilde{\mathbf{p}}_j = \mathbf{p}_j + \Delta \mathbf{p}_j$ .

**Axial-plane rotation.** Gaussian rotation is restricted to the axial plane (rotation around the superior-inferior  $Z$ -axis), again to prevent cross-slice interference and to keep each Gaussian’s spatial footprint aligned with its ray.

**Scale initialization and clamping.** All scale axes are initialized to  $\sigma_0 = 0.25$  px, close to the inter-ray spacing around the dental arch, and clamped during training to  $s_{\max} = 1.0$  px. At this ceiling, 95% of each Gaussian’s density is contained within a radius of  $2\sigma = 2.0$  px, matching the observed inter-ray distance near the teeth and ensuring Gaussians do not grow large enough to bridge anatomically distinct structures on neighbouring rays. Starting small and allowing growth lets the model first place Gaussians accurately and then expand them to fill inter-ray gaps, avoiding the degenerate all-diffuse initialization that large initial scales would produce.

**Coarse volume synthesis.** The  $N_g$  Gaussians are rasterized into a coarse volume  $\hat{V}_c \in \mathbb{R}^{H \times W \times D}$  via the differentiable R2-Gaussian voxelizer [48], which corrects an integration bias in standard 3DGS for X-ray physics:

$$\hat{V}_c(\mathbf{x}) = \sum_j \alpha_j \exp\left(-\frac{1}{2}(\mathbf{x} - \tilde{\mathbf{p}}_j)^\top \Sigma_j^{-1}(\mathbf{x} - \tilde{\mathbf{p}}_j)\right), \quad (4)$$

where  $\Sigma_j = \mathbf{R}_j \text{diag}(\mathbf{s}_j^2) \mathbf{R}_j^\top$  and  $\mathbf{R}_j$  is the rotation matrix derived from  $\mathbf{q}_j$ . Gradients flow through the voxelizer back to  $f_\phi$ , enabling end-to-end training.

### 2.5. Residual Refiner

The Gaussian coarse volume  $\hat{V}_c$  already carries the geometric structure of the generation: because all projection losses are applied directly to  $\hat{V}_c$ , the MLP is explicitly trained to solve the 3D lifting problem from the 2D conditioning signal. We additionally supervise  $\hat{V}_f$ , giving the refiner the role of incorporating population-level anatomical priors (typical jaw morphology, tooth arrangement, density distributions) learned at the dataset level, while the geometric fidelity to the input PXR is anchored in the coarse stage.

To enforce this division of responsibility we parameterize the refiner as a residual correction. A deliberately small 3D U-Net  $r_\psi$  (see Appendix B.2.1) predicts:

$$\hat{V}_f = \hat{V}_c + r_\psi(\hat{V}_c). \quad (5)$$

The refiner is intentionally kept small (3 stages, max 128 feature channels), in contrast to NeBLa’s[31] refiner with 5 stages and a 1024 channel bottleneck, which risks memorizing population-level anatomy over geometric fidelity. A large network trained on a fixed cohort risks memorizing population-level anatomy regardless of the input, prioritizing dataset statistics over the geometric constraints in the coarse volume. By limiting capacity and restricting to a residual, the network can only make small adjustments and cannot deviate substantially from the geometrically grounded Gaussian prediction, favouring generalization over memorization. The final convolutional layer is zero-initialized so that  $r_\psi$  begins as a zero correction, ensuring  $\hat{V}_f = \hat{V}_c$  early in training and gradient signal flows through the Gaussian parameters and MLP before the refiner contributes.

## 2.6. Training Objective

X-Splat is trained end-to-end with a composite loss applied independently to both  $\hat{V}_c$  and  $\hat{V}_f$  with equal stage weights. Losses are grouped into three categories calibrated after training stabilized at approximately 100 epochs: geometric projection losses ( $\approx 70\%$ ), perceptual losses ( $\approx 15\%$ ), and volumetric intensity loss ( $\approx 15\%$ ).

**Volumetric intensity loss.** MSE between prediction and ground-truth CBCT penalizes global intensity errors:

$$\mathcal{L}_{\text{rec}} = \|\hat{V} - V^*\|^2. \quad (6)$$

**Geometric projection losses.** Three complementary losses constrain the reconstructed 3D geometry. The Beer-Lambert projection loss renders  $\hat{V}$  back to a SimPX and compares it to the input:

$$\mathcal{L}_{\text{proj}} = \|\mathcal{F}(\hat{V}, \theta_0) - \mathbf{I}\|^2. \quad (7)$$

Maximum-intensity projection (MIP) losses along all three anatomical axes provide orthogonal structural supervision without requiring full volumetric alignment:

$$\mathcal{L}_{\text{mip}} = \sum_{a \in \{x, y, z\}} \|\text{MIP}_a(\hat{V}) - \text{MIP}_a(V^*)\|^2. \quad (8)$$

The multi-view DRR loss  $\mathcal{L}_{\text{mv}}$  (Eq. (11), Section 2.7) resolves front-to-back depth ambiguity by enforcing consistency across azimuthal projections.

**Perceptual losses.** Following NeBLa [31], VGG-based perceptual losses are applied to 2D projections of  $\hat{V}_f$  to encourage high-frequency anatomical detail. Perceptual supervision covers the Beer-Lambert projection, all three MIP projections, and eight representative multi-view DRR angles at

$\theta \in \{\pm 37.5^\circ, \pm 52.5^\circ, \pm 67.5^\circ, \pm 82.5^\circ\}$  selected for symmetric angular coverage:

$$\mathcal{L}_{\text{perc}} = \sum_{P \in \mathcal{P}} \|\phi_{\text{VGG}}(P(\hat{V}_f)) - \phi_{\text{VGG}}(P(V^*))\|^2, \quad (9)$$

where  $\mathcal{P}$  collects all supervised projection operators and  $\phi_{\text{VGG}}$  extracts intermediate VGG feature maps.

**Total loss.** The composite objective,

$$\mathcal{L} = \underbrace{\lambda_{\text{rec}} \mathcal{L}_{\text{rec}}}_{\approx 15\%} + \underbrace{\lambda_{\text{proj}} \mathcal{L}_{\text{proj}} + \lambda_{\text{mip}} \mathcal{L}_{\text{mip}} + \lambda_{\text{mv}} \mathcal{L}_{\text{mv}}}_{\approx 70\%} + \underbrace{\lambda_{\text{perc}} \mathcal{L}_{\text{perc}}}_{\approx 15\%}, \quad (10)$$

is summed over both  $\hat{V}_c$  and  $\hat{V}_f$  with equal stage weights. Loss weights were tuned once on a held-out validation case after training had stabilized and were kept fixed thereafter.

## 2.7. Multi-view DRR Consistency Loss

Reconstructing a 3D volume from a single 2D projection is fundamentally ill-posed: the feasibility set  $\mathcal{S} = \{V : \mathcal{F}(V, \theta_0) = I_{\theta_0}\}$  is infinite-dimensional, containing every configuration that preserves Beer-Lambert integrals along  $\theta_0$ . We resolve this with a training-time regularizer inspired by angular coverage in CT [29] and sparse-view neural rendering [14, 27], supervising the predicted volume against DRRs from  $N=31$  azimuthal angles. While a  $180^\circ$  arc is theoretically sufficient for an ideal upright patient [29], dental CBCT patients exhibit non-negligible pitch and roll, breaking projection symmetry and introducing genuine parallax beyond  $180^\circ$ ; we therefore use  $\Delta\theta=7.5^\circ$  spacing over  $\pm 112.5^\circ$  ( $225^\circ$  total), matching clinical half-scan practice [36]. Unlike prior methods supervised only along anatomical axes, these Beer-Lambert DRRs expose azimuthal views unavailable from any other loss, aimed at resolving depth and reducing geometric ambiguity. The loss penalizes any predicted volume  $\hat{V}$  whose projections diverge from the GT DRRs:

$$\mathcal{L}_{\text{mv}} = \frac{1}{N} \sum_{i=1}^N \|\mathcal{F}(\hat{V}, \theta_i) - \mathcal{F}(V^*, \theta_i)\|^2. \quad (11)$$

Gradients flow through the differentiable renderer back into the Gaussian parameters and MLP weights, penalizing configurations that satisfy the single-view loss yet produce incorrect lateral projections. Under this joint supervision the feasibility set  $\bigcap_{i=1}^N \{V : \mathcal{F}(V, \theta_i) = \mathcal{F}(V^*, \theta_i)\}$  contracts toward geometrically consistent generations, driving splats toward true tissue boundaries.

## 3. Experiments

**Dataset.** To train and evaluate, we use a subset of a publicly available ToothFairy3 [3, 22, 23] dataset. We select

Table 1. Quantitative comparison of 3D CBCT generation from a single synthesized panoramic X-ray. Intensity-based metrics (PSNR, SSIM, LPIPS) measure overall volume fidelity. Geometry-aware metrics assess spatial generation accuracy independently of absolute patient positioning: **BA-ASD** (Big Anatomy Average Surface Distance, mm  $\downarrow$ ) measures surface accuracy over five major maxillofacial structures [4]; **TVR** (Teeth Volume Recall, %  $\uparrow$ ) measures the fraction of ground-truth tooth volume reconstructed, averaged per tooth class present in the patient; **CVR** (Canal Volume Recall, %  $\uparrow$ ) measures the fraction of ground-truth mandibular canal (MC) volume reconstructed; **HV** (Hallucinated Volume, %  $\downarrow$ ) is the total volume of falsely predicted tooth structures as a fraction of the ground-truth teeth volume. Best per column in **bold**; second best underlined.  $\dagger$  - intensity metrics calculated only for arch offset sub-volume - see Fig. 4,  $\ddagger$  - uses dental arch geometry derived from GT segmentation labels (oracle geometry).

Method	Intensity-based			Geometry-aware			
	PSNR $\uparrow$	SSIM $\uparrow$	LPIPS $\downarrow$	BA-ASD $\downarrow$	TVR $\uparrow$	CVR $\uparrow$	HV $\downarrow$
X2CT-GAN [45]	19.52 <sub>1.00</sub>	66.33 <sub>3.15</sub>	0.373 <sub>0.029</sub>	58.60 <sub>15.98</sub>	25.95 <sub>23.86</sub>	1.88 <sub>2.26</sub>	4.38 <sub>8.00</sub>
R2N2 [8]	23.11 <sub>0.70</sub>	61.63 <sub>1.28</sub>	0.324 <sub>0.011</sub>	28.98 <sub>19.01</sub>	36.08 <sub>7.64</sub>	0.01 <sub>0.02</sub>	19.27 <sub>16.46</sub>
Residual CNN [11]	21.75 <sub>1.02</sub>	<u>76.00</u> <sub>2.37</sub>	<u>0.286</u> <sub>0.021</sub>	13.06 <sub>12.29</sub>	66.80 <sub>9.58</sub>	<u>27.62</u> <sub>21.28</sub>	14.95 <sub>18.25</sub>
GAN [9]	23.12 <sub>0.67</sub>	<u>67.59</u> <sub>1.96</sub>	<u>0.297</u> <sub>0.010</sub>	<u>10.60</u> <sub>16.59</sub>	70.29 <sub>10.50</sub>	9.11 <sub>7.70</sub>	14.36 <sub>15.04</sub>
NeBLa [31]	20.79 <sub>0.45</sub>	74.42 <sub>0.84</sub>	0.297 <sub>0.006</sub>	<u>35.67</u> <sub>21.97</sub>	<u>74.12</u> <sub>3.64</sub>	1.14 <sub>1.27</sub>	<u>3.99</u> <sub>5.33</sub>
Oral-3D [38]	25.93 <sub>0.44</sub> $\dagger$	86.57 <sub>1.23</sub> $\dagger$	0.162 <sub>0.019</sub> $\dagger$	47.55 <sub>18.27</sub> $\ddagger$	76.58 <sub>10.79</sub> $\ddagger$	48.35 <sub>22.73</sub> $\ddagger$	1.07 <sub>1.47</sub> $\ddagger$
<b>X-Splat (Ours)</b>	<b>23.27</b> <sub>0.91</sub>	<b>79.62</b> <sub>1.76</sub>	<b>0.259</b> <sub>0.015</sub>	<b>2.39</b> <sub>0.74</sub>	<b>84.96</b> <sub>4.51</sub>	<b>67.33</b> <sub>19.83</sub>	<b>2.96</b> <sub>5.16</sub>

scans with no more than 50% missing dentition and a full maxillofacial field of view. Each scan includes the complete anatomy of all visible teeth, from crown to root apex, with no dental structures cropped or omitted. Applying these criteria to the full ToothFairy3 release yielded 60 eligible scans with paired segmentation labels. The dataset was randomly partitioned into training (n = 45), validation (n = 5), and test (n = 10) sets, while maintaining a comparable proportion of patients with missing teeth across all subsets.

**Implementation details.** We train X-Splat exclusively on synthetic SimPX-CBCT pairs, simulating the panoramic projection from each training CBCT using Eq. (1) and the scanning geometry of Section 2.2. This yields perfectly registered input-output pairs at no acquisition cost. Matched real PXR-CBCT pairs are exceedingly rare in clinical practice, as the two modalities are seldom acquired on the same day, and verifying sub-voxel registration between them is non-trivial. All implementation details can be found in B.2.

**Evaluation metrics.** We report intensity-based metrics (PSNR, SSIM, LPIPS) and four geometry-aware metrics: Big Anatomy Average Surface Distance (BA-ASD, mm  $\downarrow$ ), Teeth Volume Recall (TVR, %  $\uparrow$ ), Canal Volume Recall (CVR, %  $\uparrow$ ), and Hallucinated Volume (HV, %  $\downarrow$ ). Full definitions are in Appendix B.4.

**Comparison with state-of-the-art.** We evaluate against six methods covering domain-specific PXR-to-3D generation (NeBLa [31], Oral-3D [38]), general volumetric prediction (R2N2 [8], Residual CNN [11], GAN [10]), and X-ray-to-CT synthesis (X2CT-GAN [45]), all trained on the same data for full craniofacial reconstruction. Oral-3D additionally requires a dental arch curve (originally from an oral photograph); we supply it from ground-truth labels, grant-

ing oracle access unavailable at real inference. Full descriptions in Appendix B.4.

**Quantitative results.** Table 1 reports results across all methods. X-Splat is best on every intensity metric (PSNR 23.27 dB, SSIM 79.62%, LPIPS 0.259), but its decisive advantage lies in the geometry-aware metrics that better capture clinically relevant fidelity.

On surface accuracy, X-Splat attains a BA-ASD of 2.39 mm over the five major craniofacial structures, 4.4 $\times$  lower than the next oracle-free method (GAN, 10.60 mm). NeBLa [31], from which we inherit the ray geometry and projection supervision, reaches 35.67 mm, 14.9 $\times$  larger. Since both methods share the same panoramic geometry, MIP loss, and MSE loss, this gap reflects both the representational advantage of explicit Gaussians and the supervision strategies they enable: direct coarse-volume losses and multi-view DRR consistency, inapplicable to NeBLa’s implicit field, leaving its large refiner under-constrained and prone to memorization over geometric fidelity.

The contrast is starkest on canal recovery (CVR): X-Splat recovers 67.33% of the MC, versus 1.14% for NeBLa and 27.62% for the only other competitive method, Residual CNN [11]. Teeth recall remains on par with the strongest baselines (84.96% TVR vs. NeBLa 74.12% and GAN [10] 70.29%), so the geometric gains do not sacrifice tooth coverage. X-Splat also hallucinates the least anatomy (2.96%), indicating that multi-view DRR regularization suppresses false positives without hurting recall.

Oral-3D [38] reports strong intensity scores, but only within the reconstructed dental-arch sub-volume under masked evaluation, with geometry-aware scores relying on oracle arch geometry from ground-truth labels. Even within

Table 2. Ablation study. *MV*: multi-view DRR consistency loss; *Crs*: supervision on the coarse Gaussian volume; *Ref*: 3D residual U-Net refiner; *Mov*: learned displacement of Gaussian anchors along rays. Geometry-aware metrics: BA-ASD - Big Anatomy Average Surface Distance mm ↓; TVR - Teeth Volume Recall % ↑; HV — Hallucinated Volume % ↓. Rows marked † evaluate the coarse volume only (no refiner). Best per column in **bold**.

Model	MV	Crs	Ref	Mov	Intensity-based			Geometry-aware		
					PSNR ↑	SSIM ↑	LPIPS ↓	BA-ASD ↓	TVR ↑	HV ↓
NeBLa [31]	-	-	✓	-	20.79 <sub>0.81</sub>	74.42 <sub>0.84</sub>	0.297 <sub>0.006</sub>	35.67 <sub>21.97</sub>	74.12 <sub>3.64</sub>	3.99 <sub>5.33</sub>
NeBLa 320-ray	-	-	✓	-	20.89 <sub>0.49</sub>	74.26 <sub>0.78</sub>	0.286 <sub>0.004</sub>	35.66 <sub>21.79</sub>	81.96 <sub>6.70</sub>	9.39 <sub>9.52</sub>
#1. w/o MV, w/o Ref, fixed†					22.97 <sub>0.62</sub>	78.75 <sub>0.92</sub>	0.291 <sub>0.007</sub>	12.45 <sub>16.14</sub>	86.38 <sub>3.59</sub>	3.49 <sub>7.18</sub>
#2. w/o MV, w/o Ref†				✓	23.08 <sub>0.66</sub>	78.92 <sub>0.99</sub>	0.289 <sub>0.007</sub>	12.98 <sub>17.04</sub>	<b>88.16</b> <sub>5.69</sub>	2.45 <sub>4.90</sub>
#3. w/o MV		✓	✓	✓	22.87 <sub>0.55</sub>	78.31 <sub>0.74</sub>	0.287 <sub>0.007</sub>	22.91 <sub>18.63</sub>	85.68 <sub>4.46</sub>	3.04 <sub>5.64</sub>
#4. w/o Crs	✓		✓	✓	<b>23.37</b> <sub>0.65</sub>	79.20 <sub>1.08</sub>	0.273 <sub>0.008</sub>	7.75 <sub>11.29</sub>	88.03 <sub>4.40</sub>	<b>1.48</b> <sub>2.46</sub>
#5. fixed anchors	✓	✓	✓		23.26 <sub>0.63</sub>	79.22 <sub>1.03</sub>	0.282 <sub>0.008</sub>	7.40 <sub>14.68</sub>	86.70 <sub>5.59</sub>	2.82 <sub>4.93</sub>
<b>X-Splat (ours)</b>	✓	✓	✓	✓	23.27 <sub>0.91</sub>	<b>79.62</b> <sub>1.76</sub>	<b>0.259</b> <sub>0.015</sub>	<b>2.39</b> <sub>0.74</sub>	84.96 <sub>4.51</sub>	2.96 <sub>5.16</sub>

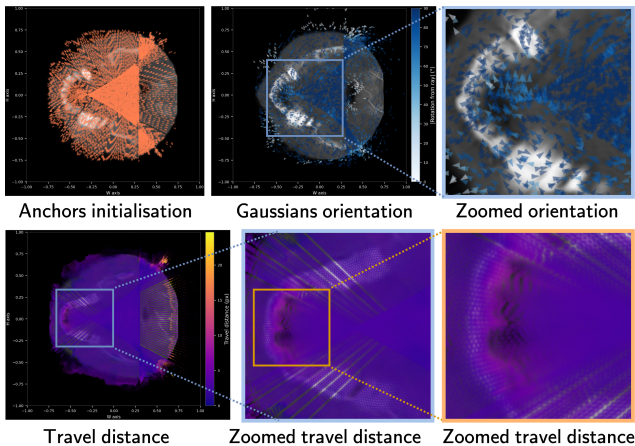


Figure 3. Gaussian primitive dynamics during inference on a test case. *Top*: anchor initialization aligns splat major axes to the ray direction (left); after training, splats rotate around the *Z*-axis (yaw only), with the zoom revealing orientations following tooth boundaries (colour: absolute rotation from ray direction in degrees). *Bottom*: travel distance of displaced Gaussians (stationary splats below 1 px hidden; colour: displacement in pixels). Gaussians near the dental arch migrate up to 10 px toward tissue boundaries, leaving voids at their origin positions. Every tenth splat per ray shown; visualization density threshold > 0.001.

this region, X-Splat surpasses it on canal recall (67.33% vs. 48.35%), recovering fine structures more completely without privileged geometric access.

**Qualitative results.** Figure 4 shows generations for a representative case. X-Splat recovers the full craniofacial anatomy of the ground-truth CBCT: cortical and trabecular bone are clearly separated, the maxillary sinuses form well-defined hypodense cavities, and the inferior alveolar nerve canal appears as a continuous tubular structure through the

mandible. The anisotropic Gaussians drive the sharp cortical boundaries, rendering the dense mineralized jaw shell as a bright high-attenuation rim in axial and coronal sections, which demands the precise ray-boundary localization that isotropic or implicit representations lack. Figure 3 visualizes the learned orientation and displacement of Gaussian primitives, confirming that splats actively rotate to align with anatomical boundaries and migrate toward high-density tissue regions during inference.

Competing methods recover coarser anatomy with less detail. NeBLa partially reconstructs bone but blurs the trabecular-cortical interface and misses the sinuses. Residual CNN is diffuse and over-smoothed with weak cortical definition, while the GAN introduces spurious high-frequency artifacts from optimising the maximum-intensity-projection loss. Oral-3D reconstructs only the dental-arch sub-volume, omitting the surrounding bony and soft-tissue anatomy (e.g. pharynx and spine).

The segmentation row highlights a key advantage: predicted tooth labels appear only where teeth exist in the ground truth, showing that X-Splat does not hallucinate dental structures in edentulous regions, a consequence of multi-view DRR regularization penalizing any density unsupported by projections from multiple directions.

**Ablation study.** Table 2 isolates the contribution of each component; extended ablation in Appendix B.5. Densifying NeBLa’s default ray count from 256 to 320 yields only marginal TVR gains, leaves BA-ASD unchanged (35.67 vs. 35.66 mm), and doubles hallucinated volume, showing that the NeRF implicit field, not ray density, is the bottleneck.

Replacing this field with fixed Gaussian anchors and no refiner alone cuts BA-ASD by 2.9× (35.67 → 12.45 mm) and raises PSNR to 22.97 dB, confirming ray-anchored anisotropic Gaussians are a far better representation for this task. Allowing ray-aligned Gaussian movement further im-

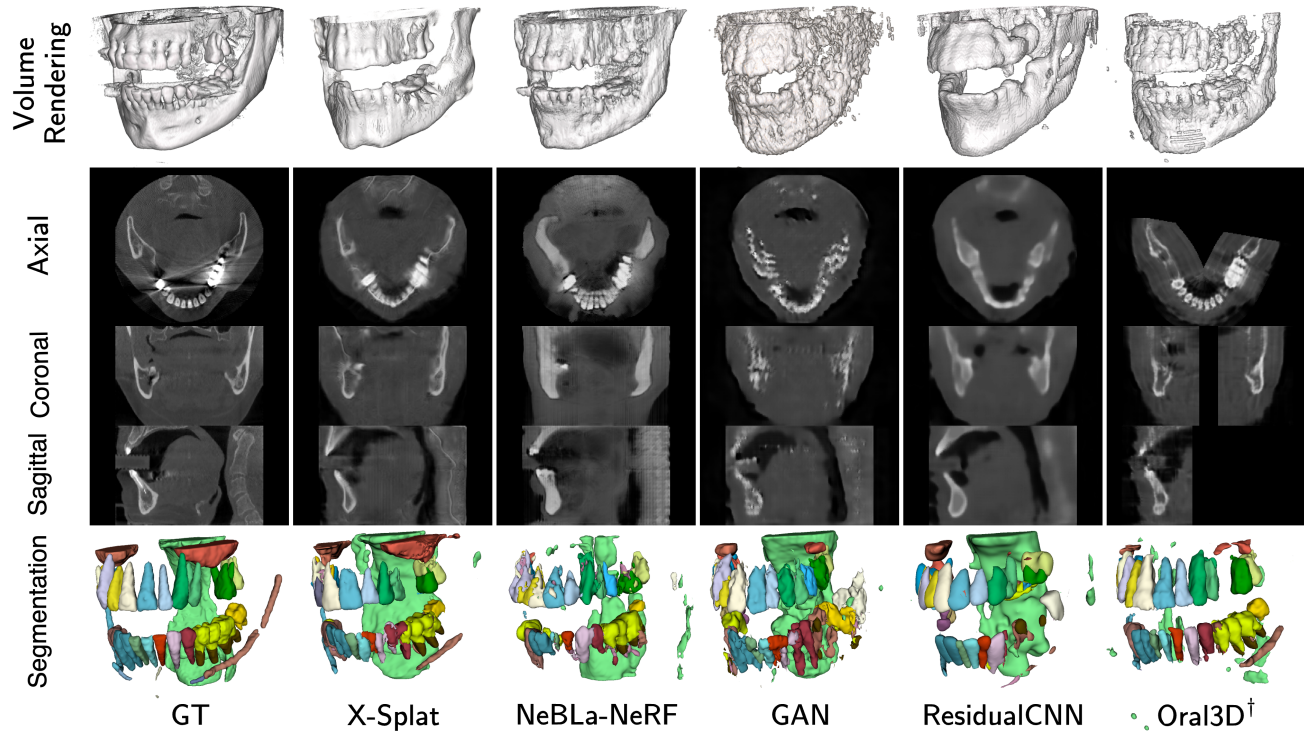


Figure 4. Qualitative comparison of 3D CBCT generation from a single panoramic X-ray. From top: volume rendering, axial, coronal, and sagittal cross-sections, and 3D segmentation. X-Splat recovers cortical and trabecular bone, maxillary sinuses, and the MC without hallucinating teeth in edentulous regions; sharp cortical boundaries are visible as bright shells in the cross-sections. Maxilla and mandible labels are hidden in the segmentation row to reveal MC and sinus structures. <sup>†</sup>Oral-3D uses ground-truth arch geometry and reconstructs only the dental arch sub-volume; surrounding anatomy is absent.

proves TVR and lowers hallucinated volume from 3.49% to 2.45%, so migration toward anatomy acts as an implicit geometric regularizer.

The refiner is only beneficial under geometric supervision. Added alone, it degrades BA-ASD from 12.98 to 22.91 mm and increases hallucinations, shifting the generation burden from the Gaussian stage to learned priors. Adding  $\mathcal{L}_{mv}$  gives the single largest gain in the ablation, restoring BA-ASD to 2.39 mm (9.6 $\times$ ) while suppressing hallucinations, confirming that multi-view better resolves depth ambiguity and constrains the refiner.

The full model attains the best BA-ASD, SSIM, and LPIPS. Its TVR (84.96%) is not the highest in isolation, variant #2 reaches 88.16%, but at the cost of BA-ASD (12.98 mm), exposing a recall–geometry trade-off. Overall, each component addresses a distinct failure mode: Gaussians provide geometric precision, movement adds expressivity and regularization, multi-view supervision enforces depth consistency, and coarse supervision anchors geometric fidelity in the Gaussian stage before refinement.

## 4. Conclusions

We present X-Splat, a feed-forward Gaussian Splatting framework for generating CBCT-like 3D maxillofacial volumes from a single panoramic radiograph, treating the known acquisition geometry as a generation scaffold: anisotropic Gaussian primitives anchored to the X-ray paths are displaced, rotated, and scaled to recover 3D anatomical structure. Coupled with Beer–Lambert reprojection, multi-view DRR supervision, and a lightweight residual refiner, this converts an otherwise highly underdetermined problem into a geometry-constrained volumetric inference task.

X-Splat improves over NeRF- and GAN-based baselines in big anatomy surface accuracy, mandibular canal recovery, and hallucination suppression, suggesting that explicit Gaussian representations are well suited to dental generation, where thin cortices, root boundaries, and canal structures require localized geometric control rather than unconstrained volumetric generation.

This work is a step toward 3D dental generation from routine panoramic imaging. While our results are consistent across both quantitative metrics and qualitative evidence, the cohort is limited to scans with full maxillofa-

cial field of view and paired segmentation labels. Generalization to more diverse patient populations and imaging conditions remains to be established. Our study uses CBCT-derived simulated panoramics, which provide paired supervision and controlled evaluation but do not fully capture the variability of real panoramic systems; future work will focus on multi-site training, real-PXR adaptation, and tissue-specialized Gaussian densification. By showing that ray-anchored Gaussian primitives can recover detailed maxillofacial structure from a single projection, X-Splat opens a path toward scalable 3D dental analysis in settings where CBCT is unavailable, impractical, or unnecessary.

## References

- [1] Ander Biguri, Tomoyuki Sadakane, Reuben Lindroos, Yi Liu, Malena Sabaté Landman, Yi Du, Manasavee Lohvithee, Stefanie Kaser, Sepideh Hatamikia, Robert Bryll, et al. Tigre v3: Efficient and easy to use iterative computed tomographic reconstruction toolbox for real datasets. *Engineering Research Express*, 7(1):015011, 2025. [12](#)
- [2] Federico Bolelli, Luca Lumetti, Shankeeth Vinayahalingam, Mattia Di Bartolomeo, Arrigo Pellacani, Kevin Marchesini, Niels Van Nistelrooij, Pieter Van Lierop, Tong Xi, Yusheng Liu, et al. Segmenting the inferior alveolar canal in cbct volumes: the toothfairy challenge. *IEEE Transactions on Medical Imaging*, 44(4):1890–1906, 2024. [2](#)
- [3] Federico Bolelli, Kevin Marchesini, Niels van Nistelrooij, Luca Lumetti, Vittorio Pipoli, Elisa Ficarra, Shankeeth Vinayahalingam, and Costantino Grana. Segmenting Maxillofacial Structures in CBCT Volume. In *IEEE/CVF Conference on Computer Vision and Pattern Recognition (CVPR)*, pages 1–10. IEEE, 2025. [5](#), [13](#), [14](#)
- [4] Federico Bolelli, Kevin Marchesini, Niels Van Nistelrooij, Luca Lumetti, Vittorio Pipoli, Elisa Ficarra, Shankeeth Vinayahalingam, and Costantino Grana. Segmenting maxillofacial structures in cbct volumes. In *Proceedings of the Computer Vision and Pattern Recognition Conference*, pages 5238–5248, 2025. [2](#), [6](#), [17](#)
- [5] Federico Bolelli, Luca Lumetti, Niels van Nistelrooij, Shankeeth Vinayahalingam, Mattia Di Bartolomeo, Kevin Marchesini, Arrigo Pellacani, Ettore Candeloro, Gabriele Rosati, Tong Xi, et al. Multi-structure segmentation in cbct volumes: The toothfairy2 challenge. *Medical Image Analysis*, page 104095, 2026. [2](#), [16](#)
- [6] Yuanhao Cai, Yixun Liang, Jiahao Wang, Angtian Wang, Yulun Zhang, Xiaokang Yang, Zongwei Zhou, and Alan Yuille. Radiative gaussian splatting for efficient x-ray novel view synthesis. In *European Conference on Computer Vision*, pages 283–299. Springer, 2024. [2](#), [12](#)
- [7] Yuanhao Cai, Jiahao Wang, Alan Yuille, Zongwei Zhou, and Angtian Wang. Structure-aware sparse-view x-ray 3d reconstruction. In *Proceedings of the IEEE/CVF conference on computer vision and pattern recognition*, pages 11174–11183, 2024. [12](#)
- [8] Christopher B Choy, Danfei Xu, JunYoung Gwak, Kevin Chen, and Silvio Savarese. 3d-r2n2: A unified approach for single and multi-view 3d object reconstruction. In *European conference on computer vision*, pages 628–644. Springer, 2016. [6](#), [12](#), [17](#)
- [9] Ian Goodfellow, Jean Pouget-Abadie, Mehdi Mirza, Bing Xu, David Warde-Farley, Sherjil Ozair, Aaron Courville, and Yoshua Bengio. Generative adversarial networks. *Communications of the ACM*, 63(11):139–144, 2020. [6](#), [17](#)
- [10] Ian J Goodfellow, Jean Pouget-Abadie, Mehdi Mirza, Bing Xu, David Warde-Farley, Sherjil Ozair, Aaron Courville, and Yoshua Bengio. Generative adversarial nets. *Advances in neural information processing systems*, 27, 2014. [1](#), [6](#), [12](#)
- [11] Philipp Henzler, Volker Rasche, Timo Ropinski, and Tobias Ritschel. Single-image tomography: 3d volumes from 2d cranial x-rays. In *Computer graphics forum*, pages 377–388. Wiley Online Library, 2018. [6](#), [12](#), [17](#)
- [12] Jonathan Ho, Ajay Jain, and Pieter Abbeel. Denoising diffusion probabilistic models. *Advances in neural information processing systems*, 33:6840–6851, 2020. [1](#)
- [13] Yicong Hong, Kai Zhang, Jiuxiang Gu, Sai Bi, Yang Zhou, Difan Liu, Feng Liu, Kalyan Sunkavalli, Trung Bui, and Hao Tan. Lrm: Large reconstruction model for single image to 3d. In *International Conference on Learning Representations*, pages 50678–50702, 2024. [12](#)
- [14] Bernhard Kerbl, Georgios Kopanas, Thomas Leimkühler, George Drettakis, et al. 3d gaussian splatting for real-time radiance field rendering. *ACM Trans. Graph.*, 42(4):139–1, 2023. [2](#), [4](#), [5](#)
- [15] Xiaoshuang Li, Mingyuan Meng, Zimo Huang, Lei Bi, Eduardo Delamare, Dagan Feng, Bin Sheng, and Jinman Kim. 3dpx: Progressive 2d-to-3d oral image reconstruction with hybrid mlp-cnn networks. In *International Conference on Medical Image Computing and Computer-Assisted Intervention*, pages 25–34. Springer, 2024. [1](#), [12](#)
- [16] Yingtai Li, Xueming Fu, Han Li, Shang Zhao, Ruiyang Jin, and S Kevin Zhou. 3dgr-ct: Sparse-view ct reconstruction with a 3d gaussian representation. *Medical Image Analysis*, 103:103585, 2025. [12](#)
- [17] Yuan Liang, Weinan Song, Jiawei Yang, Liang Qiu, Kun Wang, and Lei He. X2teeth: 3d teeth reconstruction from a single panoramic radiograph. In *International Conference on Medical Image Computing and Computer-Assisted Intervention*, pages 400–409. Springer, 2020. [1](#), [12](#)
- [18] Tianyu Lin, Xinran Li, Chuntung Zhuang, Qi Chen, Yuanhao Cai, Kai Ding, Alan Yuille, and Zongwei Zhou. Are pixel-wise metrics reliable for computerized tomography reconstruction? *Advances in Neural Information Processing Systems*, 38:33662–33708, 2026. [2](#), [12](#)
- [19] Zhentao Liu, Yu Fang, Changjian Li, Han Wu, Yuan Liu, Dinggang Shen, and Zhiming Cui. Geometry-aware attenuation learning for sparse-view cbct reconstruction. *IEEE Transactions on Medical Imaging*, 44(2):1083–1097, 2024. [1](#), [12](#)
- [20] Zhentao Liu, Huangxuan Zhao, Wenhui Qin, Zhenghong Zhou, Xinggang Wang, Wenping Wang, Xiaochun Lai, Dinggang Shen, and Zhiming Cui. 3d vessel reconstruction from sparse-view dynamic dsa images via vessel probability guided attenuation learning. *Medical Image Analysis*, page 104088, 2026. [12](#)

- [21] Xiaoxiao Long, Yuan-Chen Guo, Cheng Lin, Yuan Liu, Zhiyang Dou, Lingjie Liu, Yuexin Ma, Song-Hai Zhang, Marc Habermann, Christian Theobalt, et al. Wonder3d: Single image to 3d using cross-domain diffusion. In *Proceedings of the IEEE/CVF conference on computer vision and pattern recognition*, pages 9970–9980, 2024. [12](#)
- [22] Luca Lumetti, Vittorio Pipoli, Federico Bolelli, Elisa Ficarra, and Costantino Grana. Enhancing Patch-Based Learning for the Segmentation of the Mandibular Canal. *IEEE Access*, pages 1–12, 2024. [5](#), [13](#), [14](#)
- [23] Luca Lumetti, Zhi Qin Tan, Lorenzo Borghi, Owen Addison, Yupeng Li, Gabriele Rosati, Niels van Nistelrooij, Shankeeth Vinayahalingam, Costantino Grana, and Federico Bolelli. Toothfairy3: Scaling cbct maxillofacial segmentation to 77 classes with u-mamba2. In *Medical Image Computing and Computer Assisted Intervention – MICCAI 2026*, 2026. [5](#), [13](#), [14](#)
- [24] Wen Ma, Huikai Wu, Zikai Xiao, Yang Feng, Jian Wu, and Zuozhu Liu. Px2tooth: Reconstructing the 3d point cloud teeth from a single panoramic x-ray. In *International Conference on Medical Image Computing and Computer-Assisted Intervention*, pages 411–421. Springer, 2024. [1](#), [12](#)
- [25] David MacDonald, Sharifa Alebrahim, Edwin Yen, and Jolanta Aleksejuniene. Cone-beam computed tomographic reconstructions in the evaluation of maxillary impacted canines. *Imaging science in dentistry*, 53(2):145, 2023. [1](#)
- [26] Lanzhuji Mei, Yu Fang, Yue Zhao, Xiang Sean Zhou, Min Zhu, Zhiming Cui, and Dinggang Shen. Dtr-net: dual-space 3d tooth model reconstruction from panoramic x-ray images. *IEEE Transactions on Medical Imaging*, 43(1):517–528, 2023. [12](#)
- [27] Ben Mildenhall, Pratul P Srinivasan, Matthew Tancik, Jonathan T Barron, Ravi Ramamoorthi, and Ren Ng. Nerf: Representing scenes as neural radiance fields for view synthesis. *Communications of the ACM*, 65(1):99–106, 2021. [1](#), [5](#), [13](#)
- [28] Sumeet Minhas, Tai-Hsien Wu, Do-Gyoon Kim, Si Chen, Yi-Chu Wu, and Ching-Chang Ko. Artificial intelligence for 3d reconstruction from 2d panoramic x-rays to assess maxillary impacted canines. *Diagnostics*, 14(2):196, 2024. [1](#)
- [29] Frank Natterer. *The Mathematics of Computerized Tomography*. Society for Industrial and Applied Mathematics, Philadelphia, PA, 2001. [5](#)
- [30] Sihwa Park, Seongjun Kim, In-Seok Song, and Seung Jun Baek. 3d teeth reconstruction from panoramic radiographs using neural implicit functions. In *International Conference on Medical Image Computing and Computer-Assisted Intervention*, pages 376–386. Springer, 2023. [1](#), [12](#)
- [31] Sihwa Park, Seongjun Kim, Doeyoung Kwon, Yohan Jang, In-Seok Song, and Seung Jun Baek. Nebla: Neural beer-lambert for 3d reconstruction of oral structures from panoramic radiographs. In *Proceedings of the AAAI Conference on Artificial Intelligence*, pages 4433–4441, 2024. [1](#), [2](#), [3](#), [4](#), [5](#), [6](#), [7](#), [12](#), [13](#), [14](#), [16](#), [17](#)
- [32] Ruben Pauwels, Jilke Beinsberger, Bruno Collaert, Chrysoula Theodorakou, Jessica Rogers, Anne Walker, Lesley Cockmartin, Hilde Bosmans, Reinhilde Jacobs, Ria Bogaerts, et al. Effective dose range for dental cone beam computed tomography scanners. *European journal of radiology*, 81(2):267–271, 2012. [1](#)
- [33] Pawel Tomasz Pieta, Rasmus Juul Pedersen, Sina Borgi, Jakob Sauer Jørgensen, Jens Wenzel Andreasen, and Vedrana Andersen Dahl. Fact-gs: Fast and scalable ct reconstruction with gaussian splatting. *arXiv preprint arXiv:2604.01844*, 2026. [12](#)
- [34] Ingrid Rozylo-Kalinowska. Panoramic radiography in dentistry. In *Imaging techniques in dental radiology: acquisition, anatomic analysis and interpretation of radiographic images*, pages 43–56. Springer, 2020. [1](#)
- [35] Darius Rückert, Yuanhao Wang, Rui Li, Ramzi Idoughi, and Wolfgang Heidrich. Neat: Neural adaptive tomography. *ACM Transactions on Graphics (TOG)*, 41(4):1–13, 2022. [12](#)
- [36] William C. Scarfe and Allan G. Farman. What is cone-beam CT and how does it work? *Dental Clinics of North America*, 52(4):707–730, 2008. [5](#)
- [37] RKW Schulze and NA Drage. Cone-beam computed tomography and its applications in dental and maxillofacial radiology. *Clinical radiology*, 75(9):647–657, 2020. [1](#)
- [38] Weinan Song, Yuan Liang, Jiawei Yang, Kun Wang, and Lei He. Oral-3d: Reconstructing the 3d structure of oral cavity from panoramic x-ray. In *Proceedings of the AAAI conference on artificial intelligence*, pages 566–573, 2021. [1](#), [2](#), [6](#), [12](#), [16](#), [17](#)
- [39] Tomasz Szczepański, Michal K Grzeszczyk, Szymon Płotka, Arleta Adamowicz, Piotr Fudalej, Przemysław Korzeniowski, Tomasz Trzciniński, and Arkadiusz Sitek. Let me decode you: Decoder conditioning with tabular data. In *International Conference on Medical Image Computing and Computer-Assisted Intervention*, pages 228–238. Springer, 2024. [13](#)
- [40] Tomasz Szczepański, Szymon Płotka, Michal K Grzeszczyk, Arleta Adamowicz, Piotr Fudalej, Przemysław Korzeniowski, Tomasz Trzciniński, and Arkadiusz Sitek. Gepar3d: Geometry prior-assisted learning for 3d tooth segmentation. In *International Conference on Medical Image Computing and Computer-Assisted Intervention*, pages 218–228. Springer, 2025. [2](#), [13](#)
- [41] Tomasz Szczepański and Szymon Płotka. *Morphology-Driven Deep Watershed Transform for 3D Tooth Segmentation*, page 159–167. Springer Nature Switzerland, 2026. [2](#), [13](#)
- [42] Haoshen Wang, Zhentao Liu, Kaicong Sun, Xiaodong Wang, Dinggang Shen, and Zhiming Cui. 3d meddiffusion: A 3d medical latent diffusion model for controllable and high-quality medical image generation. *IEEE Transactions on Medical Imaging*, 2025. [1](#)
- [43] Jiale Xu, Weihao Cheng, Yiming Gao, Xintao Wang, Shenghua Gao, and Ying Shan. Instantmesh: Efficient 3d mesh generation from a single image with sparse-view large reconstruction models. *arXiv preprint arXiv:2404.07191*, 2024. [13](#)
- [44] Ruggero Rodriguez y Baena, Riccardo Beltrami, Angelo Tagliabo, Silvana Rizzo, and Saturnino-Marco Lupi. Differences between panoramic and cone beam-ct in the surgical

- evaluation of lower third molars. *Journal of Clinical and Experimental Dentistry*, 9(2):e259, 2017. [1](#)
- [45] Xingde Ying, Heng Guo, Kai Ma, Jian Wu, Zhengxin Weng, and Yefeng Zheng. X2ct-gan: reconstructing ct from biplanar x-rays with generative adversarial networks. In *Proceedings of the IEEE/CVF conference on computer vision and pattern recognition*, pages 10619–10628, 2019. [1](#), [6](#), [12](#), [17](#)
- [46] Guangming Zang, Ramzi Idoughi, Rui Li, Peter Wonka, and Wolfgang Heidrich. Intratomo: self-supervised learning-based tomography via sinogram synthesis and prediction. In *Proceedings of the IEEE/CVF International Conference on Computer Vision*, pages 1960–1970, 2021. [1](#), [12](#)
- [47] Ruyi Zha, Yanhao Zhang, and Hongdong Li. Naf: neural attenuation fields for sparse-view cbct reconstruction. In *International Conference on Medical Image Computing and Computer-Assisted Intervention*, pages 442–452. Springer, 2022. [1](#), [12](#)
- [48] Ruyi Zha, Tao Jun Lin, Yuanhao Cai, Jiwen Cao, Yanhao Zhang, and Hongdong Li.  $R^2$ -gaussian: Rectifying radiative gaussian splatting for tomographic reconstruction. *Advances in Neural Information Processing Systems*, 37:44907–44934, 2024. [2](#), [4](#), [12](#), [14](#), [15](#)

# X-Splat: Gaussian Splatting for 3D CBCT Generation from Single Panoramic Radiograph

## Supplementary Material

### A. Related Work

#### A.1. 3D generation from Panoramic Radiographs

Recovering 3D oral anatomy from a panoramic radiograph has progressed from GAN-based volumetric prediction toward physics-aware implicit representations. We organize prior work by generation scope (individual teeth vs. the complete oral volume) and by physics grounding.

**Tooth-level generation.** A first line recovers individual tooth shapes as meshes, point clouds, or occupancy fields rather than full CBCT intensities. X2Teeth [17] was the first CNN framework to reconstruct the occupancy of all teeth from a single PXR via localization and patch-wise generation sub-networks. Occudent [30] used neural implicit occupancy from shape and class embeddings, PX2Tooth [24] extended this to point clouds with a root-apex prior, and DTR-Net [26] jointly reconstructed intensities and tooth geometry in a dual space. However, all reconstruct only tooth geometry, omitting alveolar bone, the mandibular canal, the maxillary sinus, and soft tissue, and thus cannot serve as standalone tools for implant or surgical planning.

**Volumetric oral generation.** A second line recovers tooth and bony anatomy as intensity volumes. Oral-3D [38] was the first to generate a 3D oral volume from a single PXR with a GAN [10], but requires the dental arch curve as input, not available at inference, and resolves only a rectified box around it, excluding surrounding anatomy such as the spine. It further limits generation to dense tissues such as bone and teeth, omitting soft-tissue structures including the pharynx, maxillary sinuses, and the mandibular canal. 3DPX [15] improved depth inference with a hybrid MLP-CNN pyramid. Neither imposes a physics-consistent constraint linking the volume to the observed projection, nor regularizes against anatomical structure, leaving the output dependent on the learned mapping’s generalization.

**Physics-grounded generation.** NeBLa [31] is the most physically principled single-view method, synthesizing a synthetic PXR intermediate via the Beer–Lambert law and a ray-tracing neural model, with real PXR translated to synthetic style at inference. While this bridges the synthetic-to-real gap, the core generation remains limited. NeBLa voxelizes implicit NeRF densities into a coarse volume and passes it to a large volumetric refiner, applying supervision only to the final refined output. Without geometric constraints on the coarse volume, depth ambiguity may remain unresolved where it matters most, and the large refiner may favor memorization of population-level anatomy over re-

covery of input-consistent geometry. The implicit representation further risks losing sharp root boundaries and canal cortex by construction, and imposes no geometrical prior, so globally inconsistent hallucinations may arise.

#### A.2. Sparse-View Neural Volumetric Generation

A broader body of work reconstructs volumes from sparse X-ray projections, providing the representations and physical rendering models relevant here.

**NeRF-based CT.** Adapting NeRF to X-ray replaces surface-reflectance rendering with the Beer–Lambert attenuation integral. IntraTomo [46] introduced a self-supervised formulation, NeAT [35] added octree-based empty-space culling, and NAF [47] specialized CBCT with hash encodings on jaw data via TIGRE [1]. SAX-NeRF [7] added the Lineformer architecture and the X3D dataset, while geometry-aware attenuation learning [19] and its vessel-guided extension [20] back-project multi-view features for high-quality generation from 5–10 views. In all cases, multi-view projections remain a prerequisite for resolving the volume.

**Gaussian Splatting for X-ray and CT.** X-Gaussian [6] first applied 3DGS to X-ray with differentiable radiative rasterization and SfM-free initialization.  $R^2$ -Gaussian [48] corrected an integration bias in X-ray 3DGS and added a differentiable voxelizer, 3DGR-CT [16] used FBP-guided initialization, and FaCT-GS [33] showed GS benefits are largest in the sparse-view regime. Separately, anatomy-aware supervision improves clinical quality beyond pixel-wise losses: CARE [18] shows PSNR/SSIM are largely insensitive to small critical structures and adds segmentation-guided completeness penalties, but operates in a self-supervised, scene-level setting driven by multi-view reprojection and acts as a post-hoc plug-in. Together, these works establish physics-consistent GS as a competitive paradigm for sparse-view CT, offering explicit geometry, fast convergence, and direct volume extraction; yet they rely on multi-view spatial redundancy and lack dataset-level priors, so they cannot resolve the null-space of a single projection.

**Single-view generation.** Unlike per-subject sparse-view optimization, single-view generation is an ill-posed one-to-many mapping requiring strong statistical priors, motivating supervised learning on paired PXR–CBCT data. In natural images, this has been addressed by GANs [10], encoder–decoders [11], multi-view architectures [8], and cross-modal synthesis [45], and more recently by large learned priors such as Wonder3D [21], LRM [13], and In-

stantMesh [43]. The shared insight is that a prior learned from large-scale data resolves the ambiguity a single view leaves open; for X-ray, however, that prior must capture anatomical structure and geometry rather than image-space appearance.

In summary, prior PXR-to-3D methods either recover isolated tooth geometry or full volumes without physics-consistent rendering or geometric regularization; sparse-view CT methods provide the rendering tools but require multiple projections, and their supervision has been limited to scene-level settings. Combining physics-consistent Gaussian Splatting with geometry-driven supervision in the dataset-level, single-view PXR-to-CBCT regime remains open, and is the core contribution of this work.

## B. Experimental setup

### B.1. Dataset

**ToothFairy3.** We use data from ToothFairy3 [3, 22, 23], a publicly available CBCT dataset released in conjunction with the ToothFairy3 MICCAI-ODIN 2025 challenge [23]. The dataset comprises three acquisition subsets that differ in scanner and field-of-view (FoV): Set A (417 volumes) and Set C (52 volumes), both restricted to the mandibular region or limited in FoV with partially cropped maxilla, acquired to capture the inferior alveolar nerve canal; and Set B (63 volumes), acquired with a broader FoV covering the complete maxillofacial anatomy, including all upper and lower teeth from crown to root apex, the maxillary sinuses, pharynx, and surrounding bony structures. Segmentation labels follow an extended FDI World Dental Federation notation covering 77 classes: jawbones, inferior alveolar and incisive canals, maxillary sinuses, pharynx, prosthetics (bridges, crowns, implants), 32 individual teeth, and the corresponding pulp chambers (32).

**Subset selection.** Single-PXR-to-CBCT reconstruction requires a full maxillofacial field of view, as the panoramic projection integrates anatomy from both arches and surrounding structures. We therefore restrict training and evaluation to Set B and further apply two quality criteria: (i) no more than 50% missing dentition, ensuring sufficient tooth anatomy for meaningful geometric evaluation, and (ii) complete crown-to-apex visibility for all present teeth with no dental structures cropped at the volume boundary. Applying these criteria to the 63 Set B volumes yielded 60 eligible scans with paired segmentation labels. These were randomly partitioned into training ( $n=45$ ), validation ( $n=5$ ), and test ( $n=10$ ) sets, with the proportion of partially edentulous patients kept comparable across all three splits.

#### B.1.1. Segmentation Model for Geometry-Aware Evaluation

To evaluate the geometric fidelity of generated volumes we use an automated segmentation model as a structure-

level evaluator: the model is applied independently to each predicted volume and to the corresponding ground-truth CBCT, and the resulting label maps are compared to compute the geometry-aware metrics (BA-ASD, TVR, CVR, HV) and explained in more details is Appendix B.4.

We use recent method GEPAR3D [40, 41] which excels in CBCT segmentation generalization [39], a feed-forward segmentation network that unifies instance-level detection and multi-class segmentation in a single pass, adapted here to the full ToothFairy3 label space. The model was trained on full-maxillofacial FoV CBCT scans, the only subset of ToothFairy3 containing complete upper and lower arch annotations and validated on the subsets (Set A and Set C), which despite their restricted field of view provide independent anatomical coverage for the lower arch, canals, and jawbone.

As an evaluator, GEPAR3D is applied uniformly to all methods and to ground truth; any segmentation inaccuracies it introduces therefore affect all predictions consistently, preserving the validity of relative comparisons. Crucially, any missed structures produce pessimistic metric estimates: a tooth or canal volume that the evaluator fails to detect lowers TVR and CVR scores for every method equally, so reported geometry-aware improvements constitute lower bounds on true structural recovery. This conservative behaviour is particularly relevant for fine structures such as root apices, where segmentation uncertainty is highest and reported scores may underestimate true recovery.

## B.2. Implementation Details

### B.2.1. Network Architecture

**2D U-Net encoder.** The panoramic image  $I$  is processed by a 2D U-Net that produces a dense feature map  $\mathbf{F} \in \mathbb{R}^{H_p \times W_p \times 128}$  at the input resolution. All convolutional blocks use the double-convolution design (two  $3 \times 3$  convolutions per block), max-pool downsampling, bilinear upsampling, and instance normalization. Features at a given pixel location are read directly at the index corresponding to each Gaussian anchor’s ray-pixel mapping.

**Shared MLP.** A single eight-layer MLP  $f_\phi$  of width 128 is shared across all  $N_g$  anchors. For anchor  $j$ , the encoder feature  $\mathbf{F}(\mathbf{p}_j)$  and the sinusoidal positional encoding  $\text{PE}(\mathbf{p}_j)$  with  $L = 7$  frequency bands are each passed through a learned linear projection and summed to form an initial fused representation  $\mathbf{h}_0$ , queried at a single pixel following [27, 31]. Eight subsequent layers with ReLU activations process  $\mathbf{h}_0$ ; a skip connection at the network midpoint concatenates  $\mathbf{h}_0$  back into the hidden state before the second half of the network, following the NeRF residual conditioning scheme [27].  $f_\phi$  outputs the raw displacement scalar  $\hat{\delta}t_j$ , log-scale vector  $\mathbf{s}_j \in \mathbb{R}^3$ , unit quaternion  $\mathbf{q}_j \in \mathbb{R}^4$ , and scalar density  $\alpha_j$ .

**Gaussian representation.** A total of  $N_g = 6,553,600$  anisotropic 3D Gaussians are anchored along panoramic acquisition rays (128 slices  $\times$  256 rays  $\times$  200 samples, matching the ray-sample count of the SimPX renderer). All three scale axes are initialized uniformly to  $\sigma_0 = 0.25$  px and clamped throughout training to  $[0.25, 1.0]$  px. Movement is restricted to the 1-D displacement  $\delta t_j = \tanh(\hat{\delta t}_j) \cdot \delta t_{\max}$  along the anchor ray within the axial ( $XY$ ) plane, with  $\delta t_{\max} = 32$  voxels; the  $Z$ -component is held at zero to preserve the dense axial coverage. Rotation is restricted to the axial plane (rotation around the  $Z$ -axis only). Density is activated with a softplus function, and Gaussian rasterization uses the differentiable R2-Gaussian CUDA voxelizer [48].

**3D residual refiner.** The refiner  $r_\psi$  is a compact 3D U-Net with three encoder/decoder stages and feature widths  $[32, 64, 128]$ , parameterized as a residual correction  $\hat{V}_f = \hat{V}_c + r_\psi(\hat{V}_c)$ . All convolutional blocks follow the double-convolution design with strided-convolution downsampling, trilinear upsampling, and instance normalization. The final  $3 \times 3 \times 3$  convolutional layer is zero-initialized so that  $r_\psi(\hat{V}_c) = \mathbf{0}$  at the start of training, ensuring that early gradient signal flows through the Gaussian parameters and MLP before the refiner contributes.

A full summary of architectural hyperparameters is given in Table 3.

### B.2.2. SimPX Ray Geometry and Rendering

We adopt the SimPX focal-trough geometry from NeBLa [31] without modification. Table 4 lists all rendering constants. The  $K = 200$  uniformly spaced samples per ray define the anchor grid together with the  $128 \times 256$  panoramic image dimensions, yielding  $N_g = 6,553,600$  anchor positions. The Beer-Lambert rendering constants ( $I_0, \beta, p_{\max}$ ) are inherited from the NeBLa calibration and held fixed throughout training. Synthetic PXR–CBCT pairs are registered at no acquisition cost. Matched real pairs are clinically rare, and verifying sub-voxel registration between them is non-trivial. Synthetic training scales to any CBCT dataset and provides exact ground-truth supervision under a physically calibrated forward model.

### B.3. Training Details

**Dataset and preprocessing.** We use a subset of the publicly available ToothFairy3 dataset [3, 22, 23], retaining scans with no more than 50% missing dentition and a full maxillofacial field of view, where every visible tooth is fully captured from crown to root apex without cropping. Applying these criteria yielded 60 eligible CBCT volumes with paired segmentation labels, partitioned into training ( $n=45$ ), validation ( $n=5$ ), and test ( $n=10$ ) sets while maintaining a comparable proportion of partially edentulous patients across all splits.

Table 3. Architecture hyperparameters.

Hyperparameter	Value
<i>2D U-Net encoder</i>	
Output feature channels	128
Convolution blocks	double ( $3 \times 3$ )
Downsampling	max-pool
Upsampling	bilinear
Normalization	instance
<i>Shared MLP</i>	
Depth (layers)	8
Width (channels)	128
Positional encoding frequencies $L$	7
Feature query radius	single pixel
<i>Gaussian representation</i>	
Total anchors $N_g$	6,553,600
Scale type	anisotropic (3 axes)
Scale initialization $\sigma_0$	0.25 px
Scale clamp range	$[0.25, 1.0]$ px
Movement mode	1-D along ray ( $XY$ )
Max displacement $\delta t_{\max}$	32 vox
Rotation mode	axial ( $Z$ -axis only)
Density activation	softplus
Voxelizer	R2-Gaussian [48]
<i>3D residual refiner</i>	
Stages	3
Feature widths	$[32, 64, 128]$
Convolution blocks	double ( $3 \times 3 \times 3$ )
Downsampling	strided convolution
Upsampling	trilinear
Normalization	instance
Final convolution kernel	$3 \times 3 \times 3$
Final convolution initialization	zero
<i>Volume</i>	
Output shape ( $X \times Y \times Z$ )	$256 \times 256 \times 128$

All volumes are resampled isotropically from their native resolution of  $0.3 \text{ mm px}^{-1}$  to  $0.65 \text{ mm px}^{-1}$ , yielding a canonical grid of  $256 \times 256 \times 128$  voxels that covers the full maxillofacial field of view within GPU memory. Intensity volumes are resampled with trilinear interpolation. Segmentation label maps are resampled via one-hot interpolation: each class is first binarized into a separate channel, the resulting stack of binary maps is interpolated linearly, and the final label is recovered by argmax across channels. Compared to nearest-neighbor resampling, this preserves the boundaries of thin structures (root apices, mandibular canal) that could otherwise be corrupted by the coarser target grid.

X-Splat is trained exclusively on synthetic Synthetic PXR–CBCT pairs: panoramic projections are synthesized from each ground-truth CBCT using the Beer-Lambert renderer and the scanning geometry, yielding perfectly regis-

Table 4. SimPX ray geometry and rendering parameters.

Parameter	Value
Coordinate system	LPS
Rotation centres $n_c$	21
Samples per ray $K$	200
Ray-length multiplier	0.5
Angular step (molar)	0.528 rad
Angular step (default)	0.600 rad
Angular step (front)	1.509 rad
Attenuation step $\Delta s$ (ray_delta)	1.35
Render sample mode	nearest-neighbour
$I_0$	1.0
$\beta$	$7.5 \times 10^{-7}$
$p_{\max}$	0.25
HU scaling method	direct scaling

tered input–output pairs at no acquisition cost. SimPXR’s intensities are normalized by a single global physics constant  $p_{\max} = 0.25$ , the divisor already embedded in the Beer-Lambert renderer, with the zero lower bound (background air) left unchanged. Unlike per-image or per-dataset-range rescaling, dividing by a fixed constant preserves the physics-consistent correspondence between CBCT HU values and Synthetic PXR pixel intensities: the same tissue density must map to the same projected attenuation regardless of the patient, which any data-driven normalization would destroy. The value  $p_{\max} = 0.25$  is physically grounded: with the calibrated Beer-Lambert parameter  $\beta = 7.5 \times 10^{-7}$  and  $K = 200$  ray samples, the integrated log-attenuation across the full dental anatomy does not exceed  $p_{\max}$  in any scan in the dataset, so no clipping of Synthetic PXR values occurs. CBCT intensities are clipped to  $[HU_{\min}, HU_{\max}] = [0, 4000]$  (spanning air through dense enamel) and rescaled linearly to  $[0, 1]$ . The full dataset is pre-cached in memory at the start of training (`cache_rate = 1.0`).

**Multi-view DRR supervision.** During training  $N = 31$  azimuthal DRR projections are rendered at  $\Delta\theta = 7.5^\circ$  spacing over  $\pm 112.5^\circ$  ( $225^\circ$  total arc, including the  $0^\circ$  centre view). Perceptual supervision is applied to the fine volume  $\hat{V}_f$  at the eight symmetric angles  $\theta \in \{\pm 37.5^\circ, \pm 52.5^\circ, \pm 67.5^\circ, \pm 82.5^\circ\}$  (DRR indices 4, 6, 8, 12, 18, 22, 24, 26 in the ordered stack).

**Loss weights.** All losses are computed independently for the coarse volume  $\hat{V}_c$  and the refined volume  $\hat{V}_f$  and summed. Perceptual losses are applied to  $\hat{V}_f$  only. Table 5 lists all weights; note that MIP-axis weights are uniform ( $x : y : z = 1 : 1 : 1$ ).

Table 5. Loss weights for each training stage. “—” denotes a term not applied to that stage.

Loss	Symbol	Fine $\hat{V}_f$	Coarse $\hat{V}_c$
Volumetric MSE	$\lambda_{\text{rec}}$	10	5
Beer-Lambert reprojection	$\lambda_{\text{proj}}$	50	50
MIP projection (3 axes)	$\lambda_{\text{mip}}$	10	5
Multi-view DRR	$\lambda_{\text{mv}}$	150	50
Perceptual (Beer-Lambert)	$\lambda_{\text{perc,proj}}$	0.05	—
Perceptual (MIP)	$\lambda_{\text{perc,mip}}$	0.01	—
Perceptual (multi-view DRR)	$\lambda_{\text{perc,mv}}$	0.02	—

Weights were calibrated once on a held-out validation case after training had stabilized at approximately 100 epochs and were then fixed for all reported experiments.

**Optimizer and learning-rate schedule.** All parameters are trained with AdamW. Per-parameter-group overrides are used to account for the distinct roles of encoder, MLP, and refiner (Table 6); parameters not assigned to a named group fall back to the global settings. The MLP receives a modestly elevated learning rate [48], reflecting its primary responsibility for solving the 3D geometric lifting problem from the 2D conditioning signal. A cosine annealing schedule reduces every group’s learning rate from its initial value to  $\eta_{\min} = 10^{-5}$  over 500 epochs with no restarts.

Table 6. AdamW hyperparameters per parameter group. Global  $\beta_1 = 0.9$ ,  $\beta_2 = 0.999$  (PyTorch defaults).

Parameter group	Learning rate	Weight decay
Global (default)	$1 \times 10^{-3}$	$1 \times 10^{-6}$
Encoder	$1 \times 10^{-3}$	$1 \times 10^{-4}$
MLP	$1.2 \times 10^{-3}$	$1 \times 10^{-6}$
Refiner	$1 \times 10^{-3}$	$1 \times 10^{-4}$
Scheduler	cosine, $\eta_{\min} = 10^{-5}$	

**Training schedule and initialization.** Models are trained for 500 epochs with batch size 1 and random seed 42. The residual refiner is active from epoch 0. X-Splat is warm-started from a prior checkpoint that does not include the refiner; on loading, any mismatched or absent parameter keys are discarded and newly added parameters (refiner weights) are initialized from scratch. The best checkpoint is selected based on loss value, which consists of raw unscaled value of projection (MIP) and MSE 3D losses.

**Hardware and software.** All experiments are run on a single NVIDIA GPU A100 80GB with PyTorch mixed precision in `bfloat16`. cuDNN benchmark mode is enabled.

The R2-Gaussian voxelizer is compiled as a custom CUDA extension. No gradient clipping is applied.

#### B.4. Evaluation metrics

Prior reconstruction methods [31, 38] evaluate volumetric overlap using an intensity threshold to binarize predictions, a reasonable proxy when segmentation labels are unavailable. However, this approach carries two limitations that are particularly pronounced in single-view CBCT generation. First, the threshold must be chosen to separate tissue from background in predictions whose intensity distributions vary across methods, introducing a systematic bias that favors methods whose output statistics happen to align with the chosen value. Second, depth along the projection axis is inherently ambiguous in single-view reconstruction, so a geometrically plausible prediction that recovers all anatomical structures at a slightly shifted position is penalized as severely as one that misses them entirely. Critically, a model that generates anatomy close to the population mean will score highly on threshold DSC regardless of whether it reflects the input radiograph, rewarding hallucination of average anatomy over patient-specific reconstruction. The availability of dense segmentation labels in Tooth-Fairy3 enables us to move beyond this proxy. We therefore prioritize surface-distance metrics expressed in millimeters, which assess geometric fidelity directly in physical space and are largely immune to this ambiguity, alongside volume-recall and hallucination measures that capture clinically relevant completeness and specificity.

**Big Anatomy ASD** (BA-ASD, mm  $\downarrow$ ) reports the symmetric Average Surface Distance over the five major craniofacial structures  $\mathcal{K}$  (mandible, maxilla, bilateral maxillary sinuses, pharynx) [5]:

$$\text{BA-ASD} = \frac{1}{|\mathcal{K}|} \sum_{k \in \mathcal{K}} \frac{1}{2} \left( \frac{1}{|S_k|} \sum_{p \in S_k} \min_{q \in \hat{S}_k} \|p - q\|_2 + \frac{1}{|\hat{S}_k|} \sum_{q \in \hat{S}_k} \min_{p \in S_k} \|p - q\|_2 \right), \quad (12)$$

where  $S_k$  and  $\hat{S}_k$  are the ground-truth and predicted surfaces of structure  $k$ . When a structure is absent from the prediction, a finite penalty equal to half the volume diagonal is assigned following [5], ensuring all cases contribute a comparable value without requiring a binary presence threshold. **Teeth Volume Recall** (TVR, %  $\uparrow$ ) measures, for each tooth class present in the ground truth, the fraction of its expected tissue volume reconstructed by the model, averaged over all present classes; a model that reconstructs only a subset of teeth scores accordingly low, preventing partial reconstructors from appearing competitive. **Canal Volume Recall** (CVR, %  $\uparrow$ ) applies the same measure to the inferior alveolar nerve canal (mandibular nerve canal), a thin tubular structure that is clinically critical yet difficult to recover.

**Hallucinated Volume** (HV, %  $\downarrow$ ) measures the total volume of falsely predicted tooth structures for tooth classes absent from the ground truth, expressed as a fraction of the ground-truth teeth volume, directly quantifying the tendency to fabricate anatomy. Intensity-based metrics (PSNR  $\uparrow$ , SSIM  $\uparrow$ , LPIPS  $\downarrow$ ) are retained as global fidelity measures and to enable direct comparison with prior work that does not report geometry-aware evaluation.

While Section B.4 argues that overlap-based metrics are unreliable discriminators of reconstruction quality in this task, we report them here for completeness and to enable direct comparison with prior work [31, 38] that reported this criterion. Table 7 reports threshold and segmentation Dice Scores alongside the geometry-aware metrics. Thr.DSC is computed at 0.4 ( $\approx 600$  HU on the normalized  $[-1000, 3000]$  HU scale), which lies above soft tissue and evaluates dense mineralized structures only, excluding the mandibular canal, pharynx, and sinuses that X-Splat explicitly reconstructs. Seg.DSC is computed against binarized ground-truth *big anatomy* segmentation labels, directly measuring whether predicted tissue coincides with actual anatomy rather than any high-attenuation region. X-Splat achieves the best score on both metrics among oracle-free full-volume methods (45.76 and 53.68 respectively), and is the only method for which Seg.DSC exceeds Thr.DSC, an increase of 7.92 points indicating that its predictions concentrate high-attenuation tissue in anatomically consistent area. The contrasting behavior of NeBLA is instructive: its Thr.DSC of 43.41 is competitive, but Seg.DSC drops to 36.08, a fall of 7.33 points. This reversal indicates that NeBLA generates plausible high-attenuation intensities whose spatial distribution may approximate the population mean rather than the specific patient, aligning well with a fixed threshold but poorly with actual labels. The insensitivity of Thr.DSC to geometric accuracy is further illustrated by Residual CNN and NeBLA: Residual CNN achieves a  $2.7\times$  lower BA-ASD than NeBLA (13.06 vs. 35.67 mm), indicating substantially more accurate anatomical placement, yet scores 4.63 points *lower* on Thr.DSC (38.78 vs. 43.41), demonstrating that a method generating geometrically correct anatomy at a slightly shifted position is penalized more than one producing mean-anatomy at the right average location. Oral-3D exhibits the same pattern despite oracle arch geometry and evaluation restricted to the arch sub-volume: Thr.DSC of 66.61 collapses to 38.54 on Seg.DSC, suggesting that even within its privileged reconstruction region, predicted tissue does not reliably coincide with ground-truth dental anatomy. The divergence between Thr.DSC and Seg.DSC across methods confirms that a fixed intensity threshold is questionably reliable proxy for geometrical and anatomical accuracy in this task.

**Comparison with state-of-the-art.** We evaluate X-Splat

Table 7. Overlap-based comparison supplementing quantitative results table. **Thr. DSC** (%  $\uparrow$ ): volumetric overlap at intensity threshold 0.4 ( $\approx 600$  HU), as used by prior works [31, 38]; evaluates dense mineralized structures only. **Seg. DSC** (%  $\uparrow$ ): overlap against binarized ground-truth big anatomy segmentation labels, removing threshold sensitivity. **BA-ASD** (mm  $\downarrow$ ) — surface distance over five major maxillofacial structures, with a diagonal penalty for absent structures [4]; **TVR** (%  $\uparrow$ ) — fraction of ground-truth tooth volume reconstructed, averaged per present tooth class; **CVR** (%  $\uparrow$ ) — fraction of mandibular canal volume reconstructed; **HV** (%  $\downarrow$ ) — falsely predicted tooth volume as a fraction of ground-truth teeth volume. Best per column in **bold**; second best underlined.  $\dagger$  Intensity metrics computed over arch sub-volume only;  $\ddagger$  uses dental arch geometry from GT segmentation labels (oracle geometry).

Method	Overlap-based		Geometry-aware			
	Thr. DSC $\uparrow$	Seg. DSC $\uparrow$	BA-ASD $\downarrow$	TVR $\uparrow$	CVR $\uparrow$	HV $\downarrow$
X2CT-GAN [45]	16.11 <sub>13.22</sub>	18.57 <sub>7.77</sub>	58.60 <sub>15.98</sub>	25.95 <sub>23.86</sub>	1.88 <sub>2.26</sub>	4.38 <sub>8.00</sub>
R2N2 [8]	33.12 <sub>7.64</sub>	34.57 <sub>10.61</sub>	28.98 <sub>19.01</sub>	36.08 <sub>7.64</sub>	0.01 <sub>0.02</sub>	19.27 <sub>16.46</sub>
Residual CNN [11]	38.78 <sub>9.16</sub>	41.09 <sub>13.24</sub>	13.06 <sub>12.29</sub>	66.80 <sub>9.58</sub>	<u>27.62</u> <sub>21.28</sub>	14.95 <sub>18.25</sub>
GAN [9]	43.08 <sub>5.89</sub>	44.90 <sub>6.75</sub>	10.60 <sub>16.59</sub>	70.29 <sub>10.50</sub>	9.11 <sub>7.70</sub>	14.36 <sub>15.04</sub>
NeBLa [31]	<u>43.41</u> <sub>7.26</sub>	36.08 <sub>11.71</sub>	35.67 <sub>21.97</sub>	<u>74.12</u> <sub>3.64</sub>	1.14 <sub>1.27</sub>	<u>3.99</u> <sub>5.33</sub>
Oral-3D [38]	66.61 <sub>5.89</sub> <sup><math>\dagger\ddagger</math></sup>	38.54 <sub>8.96</sub> <sup><math>\dagger\ddagger</math></sup>	47.55 <sub>18.27</sub> <sup><math>\ddagger</math></sup>	76.58 <sub>10.79</sub> <sup><math>\ddagger</math></sup>	48.35 <sub>22.73</sub> <sup><math>\ddagger</math></sup>	1.07 <sub>1.47</sub> <sup><math>\ddagger</math></sup>
<b>X-Splat (Ours)</b>	<b>45.76</b> <sub>8.59</sub>	<b>53.68</b> <sub>11.39</sub>	<b>2.39</b> <sub>0.74</sub>	<b>84.96</b> <sub>4.51</sub>	<b>67.33</b> <sub>19.83</sub>	<b>2.96</b> <sub>5.16</sub>

against six representative single-view 3D generation methods. **NeBLa** [31] is the current state-of-the-art for CBCT generation from a single panoramic radiograph, combining the Beer-Lambert driven panoramic ray geometry with a NeRF-style implicit field supervision; X-Splat builds directly upon its ray geometry and projection model. **Oral-3D** [38] is a GAN-based method that reconstructs 3D oral structures from a single panoramic image by learning a flattened volumetric representation that is then geometrically deformed and interpolated back into 3D space using the dental arch curve as a spatial deformation operator. In our implementation the arch is derived from ground-truth tooth label centroids and jaw bone skeleton, constituting oracle geometric access normally not available at inference time. **R2N2** [8] reconstructs 3D shapes from images via a recurrent encoder; following [31], the recurrent connection is removed for the single-image setting. **Residual CNN** [11] employs an encoder-decoder network for volumetric generation. **GAN** [9] uses the Residual CNN as generator paired with an adversarial discriminator. **X2CT-GAN** [45] reconstructs CT volumes from biplanar X-rays, adapted here to the single-view setting. Prior panoramic generation methods, including NeBLa and Oral-3D, focus primarily on hard dental tissues such as teeth and jaw bone. We train and evaluate all methods on the full maxillofacial volume, including soft-tissue cavities and the mandibular canal, providing a more complete assessment of generation quality.

## B.5. Ablation study

Table 8 ablates Gaussian count and travel budget. Increasing  $N$  from 1.5M to 3M produces the sharpest geometry gain in this experiment: BA-ASD falls from 12.63 to

5.15 mm, indicating that at 1.5M inter-anchor gaps are wide enough that splats cannot fill the density field without approaching the scale limit, leaving regions either absent or covered by splats whose anchor features do not correspond to that location. A further doubling to 6M halves BA-ASD again (5.15  $\rightarrow$  2.39 mm) while SSIM slightly decreases (79.86  $\rightarrow$  79.62%), showing that geometry-aware metrics remain sensitive to splat density beyond the point at which intensity metrics saturate. We therefore select  $N=6M$  for the proposed model; the 3M configuration is a practical alternative under compute constraints, recovering most intensity quality at half the primitive count. *This efficiency is unavailable to implicit NeRF representations, whose sample count is fixed by the ray grid and cannot be spatially concentrated on anatomy.*

For travel distance,  $\delta t_{\max}=32$  gives the best overall balance. As we showed, most Gaussians use only a small fraction of the permitted range (Gaussian Dynamic Figure), with productive migrations concentrated as short-range adjustments toward tissue boundaries; the budget therefore acts as a regulariser rather than an active constraint. Larger values modestly reduce hallucinated volume (HV 3.86  $\rightarrow$  2.78 at  $\delta t_{\max}=48$ ) but degrade both SSIM and TVR. Since actual displacement remains well below the budget, a larger  $\delta t_{\max}$  compresses the used portion of the tanh output into a steeper region of the curve, increasing gradient sensitivity and likely destabilizing optimisation without expanding the range productively used in practice.

Scale range was not ablated independently: it is determined by the panoramic ray geometry and constitutes a design constraint rather than a tunable hyperparameter. Splats are initialized at  $1\sigma=0.25$  px and allowed to grow up to

Table 8. Ablation on test set over Gaussian count  $N$  and maximum along-ray travel distance  $\delta t_{\max}$  (pixels). Primitives are sampled uniformly, retaining every  $k$ -th splat per ray; for  $N=3\text{M}$  every second splat is retained. Shaded rows repeat the shared reference ( $N=3\text{M}$ ,  $\delta t_{\max}=32$ ); all configurations otherwise use the full X-Splat pipeline and loss weights. **X-Splat** uses  $N=6\text{M}$ ,  $\delta t_{\max}=32$ . Metric definitions follow main ablation table.

$N$	$\delta t_{\max}$	Intensity-based			Geometry-aware		
		PSNR $\uparrow$	SSIM $\uparrow$	LPIPS $\downarrow$	BA-ASD $\downarrow$	TVR $\uparrow$	HV $\downarrow$
1.5M	32	23.16 <sub>0.67</sub>	78.16 <sub>0.98</sub>	0.291 <sub>0.006</sub>	12.63 <sub>16.93</sub>	87.90 <sub>4.10</sub>	3.69 <sub>5.70</sub>
3M	32	23.24 <sub>0.72</sub>	79.86 <sub>1.09</sub>	0.268 <sub>0.007</sub>	5.15 <sub>9.24</sub>	88.66 <sub>5.37</sub>	3.86 <sub>4.38</sub>
6M	32	23.27 <sub>0.91</sub>	79.62 <sub>1.76</sub>	0.259 <sub>0.015</sub>	2.39 <sub>0.74</sub>	84.96 <sub>4.51</sub>	2.96 <sub>5.16</sub>
3M	32	23.24 <sub>0.72</sub>	79.86 <sub>1.09</sub>	0.268 <sub>0.007</sub>	5.15 <sub>9.24</sub>	88.66 <sub>5.37</sub>	3.86 <sub>4.38</sub>
3M	48	23.05 <sub>0.70</sub>	78.61 <sub>1.07</sub>	0.265 <sub>0.006</sub>	6.98 <sub>14.73</sub>	88.07 <sub>4.04</sub>	2.78 <sub>3.11</sub>
3M	64	23.17 <sub>0.70</sub>	78.21 <sub>1.06</sub>	0.281 <sub>0.006</sub>	4.66 <sub>7.36</sub>	87.99 <sub>3.54</sub>	2.81 <sub>4.70</sub>

a maximum whose  $3\sigma$  extent does not significantly overlap the nearest neighboring ray, directly preserving the per-ray PXR conditioning that underlies the method. Relaxing this bound to compensate for sparser coverage at lower  $N$  would cause splats to extend across multiple rays, so that each Gaussian’s density is no longer informed exclusively by its anchor ray feature, thus invalidating the core conditioning mechanism rather than ablating  $N$  in isolation. At  $N=1.5\text{M}$ , some inter-ray gaps cannot be filled without splats exceeding the scale bound. Along-ray displacement can reposition splats within their ray but cannot place density between rays, leaving those regions either absent from the density field or covered by splats whose anchor features do not correspond to that location. Both failure modes are tolerated by intensity-based metrics, which average over the full volume and have low sensitivity to localized spatial errors, but are directly exposed by BA-ASD, which measures surface accuracy and captures the sharp geometric degradation at  $N=1.5\text{M}$ . The appropriate remedy is denser sampling, not larger splats, which is precisely what the  $N=3\text{M}$  and  $N=6\text{M}$  configurations provide. Notably, even at  $N=1.5\text{M}$  the model reconstructs anatomically coherent volumes, PSNR of 23.16 dB and TVR of 87.90% remain competitive, indicating that the ray-anchored Gaussian representation is robust to moderate reductions in primitive count, with geometric precision rather than overall generation quality being the primary casualty of sparser coverage.

## B.6. Qualitative Results

Figures 6 and 7 extend the qualitative comparison of the main paper to two additional test cases. X-Splat is the only method to recover the mandibular canal as a continuous tubular structure, visible as a curved hypodense channel in the sagittal cross-section and as a distinct labelled object in the 3D segmentation. Competing methods either omit the canal entirely or produce disconnected fragments, consistent with the reported CVR gap. The maxillary si-

nuses appear as clearly defined bilateral hypodense cavities in the GT Sagittal view; X-Splat reproduces partially their shape and symmetry, while NeBLa-NeRF and Residual CNN fill the sinus region with diffuse intermediate intensity and GAN introduces artifacts that obscure the boundary entirely. Oral-3D, despite oracle arch access, reconstructs only the dental sub-volume and produces no sinus anatomy. Despite strong overall anatomy recovery, X-Splat struggles to precisely reconstruct root apices, where the fine geometry may exceed the resolution of the current splat density; larger training datasets and feed-forward adaptive densification of Gaussian primitives near high-curvature boundaries remain directions for future work.

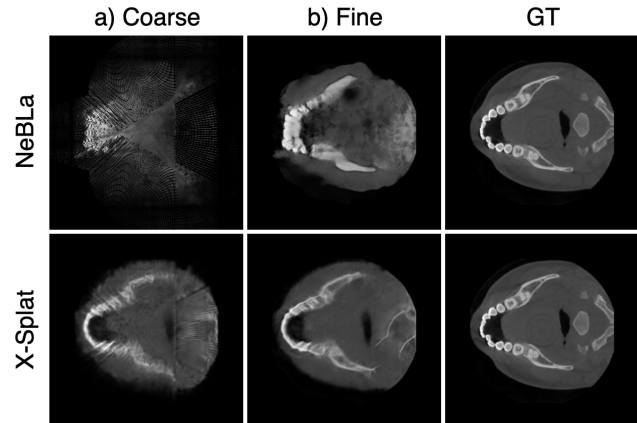


Figure 5. Axial cross-sections of coarse (a) and refined (b) volumes alongside ground truth. NeBLa’s coarse volume exhibits inter-ray gaps and little anatomical structure, placing geometry recovery almost entirely on the refiner. X-Splat’s Gaussian voxelizer produces a continuous coarse volume with the dental arch already localized and mandibular curvature resolved; the residual refiner then performs targeted correction rather than complete reconstruction, indicating that geometric information is preserved through the pipeline rather than invented by the refiner.

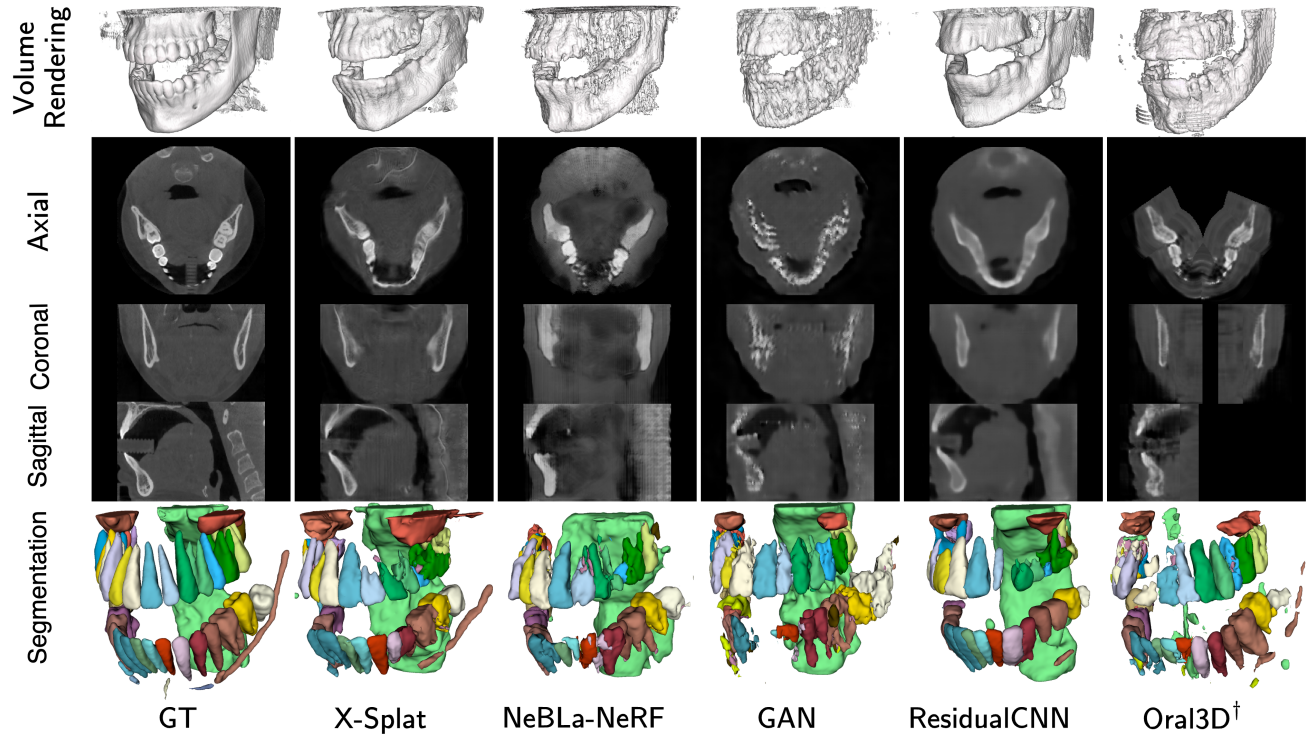


Figure 6. Supplementary qualitative comparison, case ID 027. <sup>†</sup>Oral-3D uses oracle arch geometry.

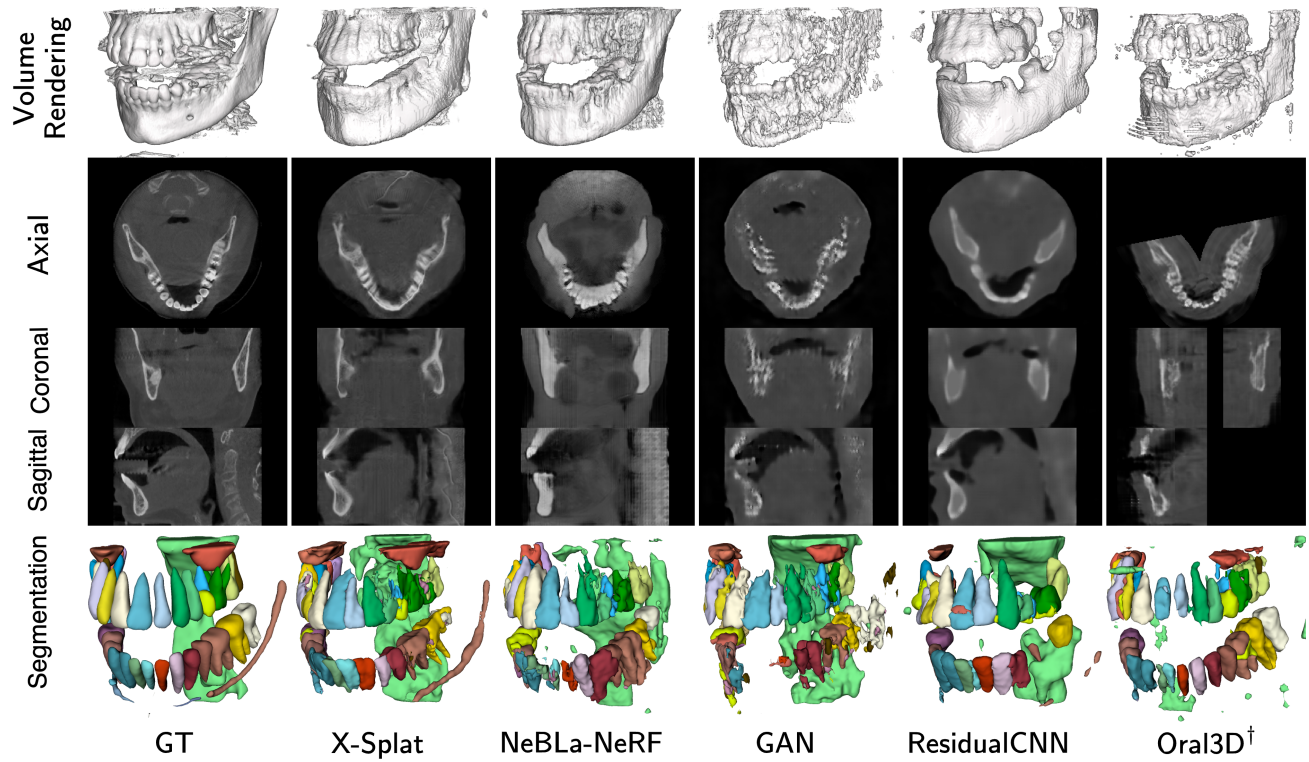


Figure 7. Supplementary qualitative comparison, case ID 030. <sup>†</sup>Oral-3D uses oracle arch geometry.